

---

# Bayesian Pose Graph Optimization via Bingham Distributions and Tempered Geodesic MCMC

---

Tolga Birdal<sup>1,2</sup> Umut Şimşekli<sup>3</sup> M. Onur Eken<sup>1,2</sup> Slobodan Ilic<sup>1,2</sup>

<sup>1</sup> CAMP Chair, Technische Universität München, 85748, München, Germany

<sup>2</sup> Siemens AG, 81739, München, Germany

<sup>3</sup> LTCI, Télécom ParisTech, Université Paris-Saclay, 75013, Paris, France

## Abstract

We introduce Tempered Geodesic Markov Chain Monte Carlo (TG-MCMC) algorithm for initializing pose graph optimization problems, arising in various scenarios such as SFM (structure from motion) or SLAM (simultaneous localization and mapping). TG-MCMC is first of its kind as it unites global non-convex optimization on the spherical manifold of quaternions with posterior sampling, in order to provide both reliable initial poses and uncertainty estimates that are informative about the quality of solutions. We devise theoretical convergence guarantees and extensively evaluate our method on synthetic and real benchmarks. Besides its elegance in formulation and theory, we show that our method is robust to missing data, noise and the estimated uncertainties capture intuitive properties of the data.

## 1 Introduction

The ability to navigate autonomously is now a key technology in self driving cars, unmanned aerial vehicles (UAV), robot guidance, augmented reality, 3D digitization, sensory network localization and more. This ubiquitous appliance is due to the fact that vision sensors can provide cues to directly solve 6DoF pose estimation problem and do not necessitate external tracking input, such as imprecise GPS, to ego-localize. Many of the problems in these domains can now be addressed by tailor-made pipelines such as SLAM (Simultaneous Localization and Mapping), SfM (Structure From Motion) or multi robot localization (MRL) [1, 2]. Nowadays, thanks to the resulting reliable estimates of rotations and translations, many of these pipelines exploit some form of an optimization, such as bundle adjustment (BA) [3] or 3D global registration [4, 5], that can globally consider the acquired measurements [6]. Holistically, these methods belong to the family of *pose graph optimization* (PGO) [7]. Unfortunately, many of PGO post-processing stages, which take in to account both camera poses and 3D structure, are too costly for online or even soft-realtime operation. This bottleneck demands good solutions for PGO initialization, that can relieve the burden of the joint optimization.

In this paper, we address the particular problem of initializing PGO, in which multiple local measurements are fused into a globally consistent estimate, without resorting to the costly bundle adjustment or optimization that uses structure. In specifics, let us consider a finite simple directed graph  $G = (V, E)$ , where vertices correspond to reference frames and edges to the available relative measurements as shown in Figures 1(a), 1(b). Both vertices and edges are labeled with rigid motions representing absolute and relative poses, respectively. Each absolute pose is described by a homogeneous transformation matrix  $\{\mathbf{M}_i \in SE(3)\}_{i=1}^n$ . Similarly, each relative orientation is expressed as the transformation between frames  $i$  and  $j$ ,  $\mathbf{M}_{ij}$ , where  $(i, j) \in E \subset [n] \times [n]$ . The labeling of the edges is such that if  $(i, j) \in E$ , then  $(j, i) \in E$  and  $\mathbf{M}_{ij} = \mathbf{M}_{ji}^{-1}$ . Hence, we consider  $G$  to be undirected. With a convention as shown in Figure 1(c), the link between absolute and relative transformations is encoded by the *compatibility constraint*:

$$\mathbf{M}_{ij} \approx \mathbf{M}_j \mathbf{M}_i^{-1}, \forall i \neq j \quad (1)$$

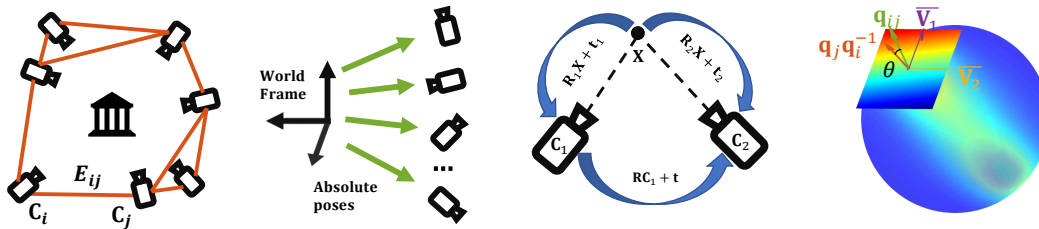


Figure 1: From left to right: (a) Initial pose graph of relative poses. (b) Absolute poses w.r.t. common reference frame. (c) Convention used to describe the pairwise relationships. (d) A sample Bingham distribution and the rotational components.

Primarily motivated by Govindu et. al. [8], *rigid-motion synchronization* initializes PGO by computing an estimate of the vertex labels  $M_i$  (absolute poses) given enough measurements of the ratios  $M_{ij}$ . In other words, it tries to find the absolute poses that best fit the relative pairwise measurements. Typically, in order to remove the gauge freedom, one of the poses is set to identity  $M_0 = \mathbf{I}$  and the problem reduces to recovering  $n - 1$  absolute poses. The solution is the state of the art method to initialize, say SfM [1, 9, 10] thanks to the good quality of the estimates.

The PGO problem is often formed as non-convex optimization problems, opening up room for different formulations and approaches. Direct methods try to compute a good initial solution [11, 9, 12, 13], which are then refined by iterative techniques [14, 15]. Robustness to outlier relative pose estimates is also crucial for a better solution [16, 17, 10, 18, 2]. The structure of our peculiar problem allows for global optimization, when isotropic noise is assumed and under reasonable noise levels as well as well connected graph structures [11, 19, 20, 21, 22, 23]. It is also noteworthy that, even though the problem has been previously handled with statistical approaches [24], up until now, to the best of our knowledge, estimation of uncertainties in PGO initialization are never truly considered.

In this paper, we look at the graph optimization problem from a probabilistic point of view. We begin by representing the problem on the Cartesian product of the true Riemannian manifold of quaternions and Euclidean manifold of translations. We model rotations with Bingham distributions [25] and translation with Gaussians. The probabilistic framework provides two important features: (i) we can align the modes of the data (relative motions) with the posterior parameters, (ii) we can quantify the uncertainty of our estimates by using the posterior predictive distributions. In order to achieve these goals, we come up with efficient algorithms both for maximum a-posteriori (MAP) estimation and posterior sampling: ‘tempered’ geodesic Markov Chain Monte Carlo (TG-MCMC). Controlled by a single parameter, TG-MCMC can either work as a standard MCMC algorithm that can generate samples from a Bayesian posterior, whose entropy, or covariance, as well as the samples themselves, provide necessary cues for uncertainty estimation - both on camera poses and possibly on the 3D structure, or it can work as an optimization algorithm that is able to generate samples around *the global optimum* of the MAP estimation problem. In this perspective, TG-MCMC bridges the gap between geodesic MCMC (gMCMC) [26] and non-convex optimization, as we will theoretically present. In a nutshell, our contributions are as follows:

- Novel probabilistic model using Bingham distributions in pose averaging for the first time,
- Tempered gMCMC: Novel tempered Hamiltonian Monte Carlo (HMC) [27, 28, 29] algorithm for global optimization and sampling on the manifolds using the known geodesic flow,
- Theoretical understanding and convergence guarantees for the devised algorithm,
- Strong experimental results justifying the validity of the approach.

## 2 Preliminaries and Technical Background

**Notation and definitions:**  $x \in \mathbb{R}$  is a scalar. We denote vectors by lower case bold letters  $\mathbf{x} = (x_1 \cdots x_N) \in \mathbb{R}^N$ . A square matrix  $\mathbf{X} = (X_{ij}) \in \mathbb{R}^{N \times N}$ .  $\mathbf{I}_{N \times N}$  is the identity matrix. Rotations belong to the special orthogonal group  $\mathbf{R} \in SO(3)$ . With translations  $\mathbf{t} \in \mathbb{R}^3$ , they form the 3D special Euclidean group  $SE(3)$ . We also define an  $m$ -dimensional *Riemannian manifold*  $\mathcal{M}$ , endowed with a *Riemannian metric*  $\mathbf{G}$  to be a smooth curved space, equipped with the inner product  $\langle \mathbf{u}, \mathbf{v} \rangle_x = \mathbf{u}^T \mathbf{G} \mathbf{v}$  in the tangent space  $\mathcal{T}_x \mathcal{M}$ , embedded in an ambient higher-dimensional Euclidean

space  $\mathbb{R}^n$ . One such manifold is the unit hypersphere in  $\mathbb{R}^d$ :  $\mathbb{S}^{d-1} = \{\mathbf{x} \in \mathbb{R}^d : \|\mathbf{x}\| = 1\} \subset \mathbb{R}^d$ . A vector  $\mathbf{v}$  is said to be *tangent* to a point  $\mathbf{x} \in \mathcal{M}$  if  $\mathbf{x}^T \mathbf{v} = 0$ . A tangent space is the set  $\mathcal{T}_x$  of all such vectors:  $\mathcal{T}_x = \{\mathbf{v} \in \mathbb{R}^d : \mathbf{x}^T \mathbf{v} = 0\}$ . We define the geodesic on the manifold to be a constant speed, length minimizing curve between  $\mathbf{x}, \mathbf{y} \in \mathcal{M}$ ,  $\gamma : [0, 1] \rightarrow \mathcal{M}$ , with  $\gamma(0) = \mathbf{x}$  and  $\gamma(1) = \mathbf{y}$ .

**Quaternions:** A *quaternion*  $\mathbf{q}$  is an element of Hamilton algebra  $\mathbb{H}$ , extending the complex numbers with three imaginary units  $\mathbf{i}, \mathbf{j}, \mathbf{k}$  in the form  $\mathbf{q} = q_1 \mathbf{1} + q_2 \mathbf{i} + q_3 \mathbf{j} + q_4 \mathbf{k} = (q_1, q_2, q_3, q_4)^T$ , with  $(q_1, q_2, q_3, q_4)^T \in \mathbb{R}^4$  and  $\mathbf{i}^2 = \mathbf{j}^2 = \mathbf{k}^2 = \mathbf{ijk} = -\mathbf{1}$ . We also write  $\mathbf{q} := [a, \mathbf{v}]$  with the scalar part  $a = q_1 \in \mathbb{R}$  and the vector part  $\mathbf{v} = (q_2, q_3, q_4)^T \in \mathbb{R}^3$ . The conjugate  $\bar{\mathbf{q}}$  of the quaternion  $\mathbf{q}$  is given by  $\bar{\mathbf{q}} := q_1 - q_2 \mathbf{i} - q_3 \mathbf{j} - q_4 \mathbf{k}$ . A versor or *unit quaternion*  $\mathbf{q} \in \mathbb{H}_1$  with  $1 \stackrel{!}{=} \|\mathbf{q}\| := \mathbf{q} \cdot \bar{\mathbf{q}}$  and  $\mathbf{q}^{-1} = \bar{\mathbf{q}}$ , gives a compact and numerically stable parametrization to represent orientation of objects in  $\mathbb{S}^3$ , avoiding gimbal lock and singularities [30, 31]. Identifying antipodal points  $\mathbf{q}$  and  $-\mathbf{q}$  with the same element, the unit quaternions form a double covering group of  $SO(3)$ . The non-commutative multiplication of two quaternions  $\mathbf{p} := [p_1, \mathbf{v}_p]$  and  $\mathbf{r} := [r_1, \mathbf{v}_r]$  is defined to be  $\mathbf{p} \otimes \mathbf{r} = [p_1 r_1 - \mathbf{v}_p \cdot \mathbf{v}_r, p_1 \mathbf{v}_r + r_1 \mathbf{v}_p + \mathbf{v}_p \times \mathbf{v}_r]$ . For simplicity we use  $\mathbf{p} \otimes \mathbf{r} := \mathbf{p} \cdot \mathbf{r} := \mathbf{pr}$ .

**Manifold of quaternions:** Unit quaternions form a hyperspherical manifold,  $\mathbb{S}^3$ , that is an embedded Riemannian submanifold of  $\mathbb{R}^4$ . This forms a Hausdorff space, where each point has an open neighborhood homeomorphic to the open N-dimensional disc, called an N-manifold. Due to the topology of the sphere, there is no unique way to find a globally covering coordinate patch. It is hence common to use local exponential and logarithmic maps that can be sphere-specifically defined as:  $\text{Exp}(\mathbf{x}, \mathbf{v}) = \mathbf{x} \cos(\theta) + \mathbf{v} \sin(\theta)/\theta$ , where  $\mathbf{v}$  denotes a tangent vector to  $\mathbf{x}$ . This property decorates quaternions with a known analytic geodesic flow, given by [26]:

$$[\mathbf{x}(t) \quad \mathbf{v}(t)] = [\mathbf{x}(0) \quad \mathbf{v}(0)] \begin{bmatrix} 1 & 0 \\ 0 & 1/\alpha \end{bmatrix} \begin{bmatrix} \cos(\alpha t) & -\sin(\alpha t) \\ \sin(\alpha t) & \cos(\alpha t) \end{bmatrix} \begin{bmatrix} 1 & 0 \\ 0 & \alpha \end{bmatrix} \quad (2)$$

where  $\alpha \triangleq \|\mathbf{v}(0)\|$ . It is also useful to think about a quaternion as the normal vector to itself, due to the unitness of the hypersphere. By this property, projection onto  $\mathcal{T}_x$  reads  $P(\mathbf{x}) = \mathbf{I} - \mathbf{x}\mathbf{x}^T$  [26].

**The Bingham Distribution:** Derived from a zero-mean Gaussian, the Bingham distribution [25] is an antipodally symmetric probability distribution conditioned to lie on  $\mathbb{S}^{d-1}$  with probability density function (PDF)  $\mathcal{B} : \mathbb{S}^{d-1} \rightarrow \mathbb{R}$ :

$$\mathcal{B}(\mathbf{x}; \mathbf{\Lambda}, \mathbf{V}) = (1/F) \exp(\mathbf{x}^T \mathbf{V} \mathbf{\Lambda} \mathbf{V}^T \mathbf{x}) = (1/F) \exp\left(\sum_{i=1}^d \lambda_i (\mathbf{v}_i^T \mathbf{x})^2\right) \quad (3)$$

where  $\mathbf{V} \in \mathbb{R}^{d \times d}$  is an orthogonal matrix ( $\mathbf{V}\mathbf{V}^T = \mathbf{V}^T\mathbf{V} = \mathbf{I}_{d \times d}$ ) describing the orientation,  $\mathbf{\Lambda} = \text{diag}(0, \lambda_1, \dots, \lambda_{d-1}) \in \mathbb{R}^{d \times d}$  with  $0 \geq \lambda_1 \geq \dots \geq \lambda_{d-1}$  is the concentration matrix, and  $F$  is a normalization constant. With this formulation, the mode of the distribution is obtained as the first column of  $\mathbf{V}$ . The antipodal symmetry of the PDF makes it amenable to explain the topology of quaternions, i. e.,  $\mathcal{B}(\mathbf{x}; \cdot) = \mathcal{B}(-\mathbf{x}; \cdot)$  holds for all  $\mathbf{x} \in \mathbb{S}^{d-1}$ . When  $d = 4$  and  $\lambda_1 = \lambda_2 = \lambda_3$ , it is safe to write  $\mathbf{\Lambda} = \text{diag}([1, 0, 0, 0])$ . In this case, the logarithm of the Bingham density reduces to the dot product of two quaternions  $\mathbf{q}_1 \triangleq \mathbf{x}$  and the mode of the distribution, say  $\bar{\mathbf{q}}_2$ . For rotations, this induces a metric,  $d_{\text{bingham}} = (\mathbf{q}_1 \cdot \bar{\mathbf{q}}_2)^2 = \cos(\theta/2)^2$ , that is closely related to the true Riemannian distance  $d_{\text{riemann}} = \|\log(\mathbf{R}_1 \mathbf{R}_2^T)\| \triangleq 2\arccos(|\mathbf{q}_1 \bar{\mathbf{q}}_2|) \triangleq 2\arccos(\sqrt{d_{\text{bingham}}})$ . Bingham distributions have been extensively used to represent distributions on quaternions [32, 33, 34]; however, to the best of our knowledge, never for the problem at hand.

### 3 The Proposed Model

We now describe our proposed model for PGO initialization. We consider the situation where we observe a set of noisy pairwise poses  $\mathbf{M}_{ij}$ , represented by *augmented quaternions* as  $\{\mathbf{q}_{ij} \in \mathbb{S}^3 \subset \mathbb{R}^4, \mathbf{t}_{ij} \in \mathbb{R}^3\}$ . The indices  $(i, j) \in E$  run over the edges the graph. We assume that the observations  $\{\mathbf{q}_{ij}, \mathbf{t}_{ij}\}_{(i,j) \in E}$  are generated by a probabilistic model that has the following hierarchical structure:

$$\mathbf{q}_i \sim p(\mathbf{q}_i), \quad \mathbf{t}_i \sim p(\mathbf{t}_i), \quad \mathbf{q}_{ij} | \cdot \sim p(\mathbf{q}_{ij} | \mathbf{q}_i, \mathbf{q}_j), \quad \mathbf{t}_{ij} | \cdot \sim p(\mathbf{t}_{ij} | \mathbf{q}_i, \mathbf{q}_j, \mathbf{t}_i, \mathbf{t}_j), \quad (4)$$

where the *latent variables*  $\{\mathbf{q}_i \in \mathbb{S}^3\}_{i=1}^n$  and  $\{\mathbf{t}_i \in \mathbb{R}^3\}_{i=1}^n$  denote the true values of the *absolute poses* and *absolute translations* with respect to a common origin, corresponding to  $\mathbf{M}_i$  of Eq. 1. Here,  $p(\mathbf{q}_i)$  and  $p(\mathbf{t}_i)$  denote the *prior distributions* of the latent variables, and the product of the densities  $p(\mathbf{q}_{ij} | \cdot)$  and  $p(\mathbf{t}_{ij} | \cdot)$  form the *likelihood function*.

By respecting the natural manifolds of the latent variables, we choose the following prior model:  $\mathbf{q}_i \sim \mathcal{B}(\Lambda_p, \mathbf{V}_p)$ ,  $\mathbf{t}_i \sim \mathcal{N}(\mathbf{0}, \sigma_p^2 \mathbf{I})$  where  $\Lambda_p$ ,  $\mathbf{V}_p$ , and  $\sigma_p^2$  are the prior model parameters, which are assumed to be known. We then choose the following model for the observed variables:

$$\mathbf{q}_{ij} | \mathbf{q}_i, \mathbf{q}_j \sim \mathcal{B}(\Lambda, \mathbf{V}(\mathbf{q}_j \bar{\mathbf{q}}_i)), \quad \mathbf{t}_{ij} | \mathbf{q}_i, \mathbf{q}_j, \mathbf{t}_i, \mathbf{t}_j \sim \mathcal{N}(\boldsymbol{\mu}_{ij}, \sigma^2 \mathbf{I}), \quad (5)$$

where  $\Lambda$  is a fixed,  $\mathbf{V}$  is a matrix-valued function that will be defined in the sequel;  $\boldsymbol{\mu}_{ij}$  denotes the expected value of  $\mathbf{t}_{ij}$  provided that the values of the relevant latent variables  $\mathbf{q}_i, \mathbf{q}_j, \mathbf{t}_i, \mathbf{t}_j$  are known, and has the form:  $\boldsymbol{\mu}_{ij} \triangleq \mathbf{t}_j - (\mathbf{q}_j \bar{\mathbf{q}}_i) \mathbf{t}_i (\mathbf{q}_i \bar{\mathbf{q}}_j)$ . With this modeling strategy, we are expecting that  $\mathbf{t}_{ij}$  would be close to the true translation  $\boldsymbol{\mu}_{ij}$  that is a deterministic function of the absolute poses. Our strategy also lets  $\mathbf{t}_{ij}$  differ from  $\boldsymbol{\mu}_{ij}$  and the level of this flexibility is determined by  $\sigma^2$ .

Constructing Bingham distribution on any given mode  $\mathbf{q} \in \mathbb{S}^3$  requires finding a frame bundle  $\mathbb{S}^3 \rightarrow \mathcal{F}\mathbb{S}^3$  composed of the unit vector (the mode) and its orthonormals. Being *parallelizable* ( $d = 1, 2, 4$  or  $8$ ), manifold of unit quaternions enjoys an injective homomorphism to the orthonormal matrix ring composed of the orthonormal basis [35]. Thus, we define  $\mathbf{V} : \mathbb{S}^3 \mapsto \mathbb{R}^{4 \times 4}$  as follows:

$$\mathbf{V}(\mathbf{q}) \triangleq \begin{bmatrix} q_1 & -q_2 & -q_3 & q_4 \\ q_2 & q_1 & q_4 & q_3 \\ q_3 & -q_4 & q_1 & -q_2 \\ q_4 & q_3 & -q_2 & -q_1 \end{bmatrix}. \quad \begin{array}{l} \text{It is easy to verify that } \mathbf{V}(\mathbf{q}) \text{ is orthonormal for every } \mathbf{q} \in \mathbb{S}^3. \\ \mathbf{V}(\mathbf{q}) \text{ further gives a convenient notation for representing} \\ \text{quaternions as matrices paving the way to linear operations,} \\ \text{such as quaternion multiplication or orthonormalization with-} \\ \text{out pesky Gram-Schmidt processes. By using the definition of } \mathbf{V}(\mathbf{q}) \text{ and assuming that the diagonal} \\ \text{entries of } \Lambda \text{ are sorted in decreasing order, we have the following property:} \end{array}$$

$$\arg \max_{\mathbf{q}_{ij}} \{p(\mathbf{q}_{ij} | \mathbf{q}_i, \mathbf{q}_j) = \mathcal{B}(\Lambda, \mathbf{V}(\mathbf{q}_j \bar{\mathbf{q}}_i))\} = \mathbf{q}_j \bar{\mathbf{q}}_i. \quad (6)$$

Similar to the proposed observation model for the relative translations, given the true poses  $\mathbf{q}_i, \mathbf{q}_j$ , this modeling strategy sets the most likely value of the relative pose to the deterministic value  $\mathbf{q}_j \bar{\mathbf{q}}_i$ , and also lets  $\mathbf{q}_{ij}$  differ from this value up to the extent determined by  $\Lambda$ . This configuration is illustrated in Fig 1(d).

Representing  $SE(3)$  in the form of a quaternion-translation parameterization, we can now formulate the motion-synchronization problem as a probabilistic inference problem. In particular we are interested in the following two quantities:

1. The maximum a-posteriori (MAP) estimate:  $(\mathbf{Q}^*, \mathbf{T}^*) = \arg \max_{\mathbf{Q}, \mathbf{T}} p(\mathbf{Q}, \mathbf{T} | \mathcal{D}) =$

$$\arg \max_{\mathbf{Q}, \mathbf{T}} \left( \sum_{(i,j) \in E} \{ \log p(\mathbf{q}_{ij} | \mathbf{Q}, \mathbf{T}) + \log p(\mathbf{t}_{ij} | \mathbf{Q}, \mathbf{T}) \} + \sum_i \log p(\mathbf{q}_i) + \sum_i \log p(\mathbf{t}_i) \right), \quad (7)$$

where  $\mathcal{D} \equiv \{\mathbf{q}_{ij}, \mathbf{t}_{ij}\}_{(i,j) \in E}$  denotes the observations,  $\mathbf{Q} \equiv \{\mathbf{q}_i\}_{i=1}^n$  and  $\mathbf{T} \equiv \{\mathbf{t}_i\}_{i=1}^n$ .

2. The full posterior distribution:  $p(\mathbf{Q}, \mathbf{T} | \mathcal{D}) \propto p(\mathcal{D} | \mathbf{Q}, \mathbf{T}) \times p(\mathbf{Q}) \times p(\mathbf{T})$ .

Both of these problems are very challenging and cannot be directly addressed by standard methods such as gradient descent (problem 1) or standard MCMC methods (problem 2). The difficulty in these problems is mainly originated by the fact that the posterior density is non-log-concave (i.e. the negative log-posterior is non-convex) and any algorithm that aims at solving one of these problems should be able to operate in the particular manifold of this problem, that is  $(\mathbb{S}^3)^n \times \mathbb{R}^{3n} \subset \mathbb{R}^{7n}$ .

## 4 Tempered Geodesic Monte Carlo for Pose Graph Optimization

**Connection between sampling and optimization:** In a recent study [36], Liu et al. proposed the stochastic gradient geodesic Monte Carlo (SG-GMC) as an extension to [26] and provided a practical posterior sampling algorithm for the problems that are defined on manifolds whose geodesic flows are analytically available. Since our augmented quaternions form such a manifold<sup>1</sup>, we can use this algorithm for generating (approximate) samples from the posterior distribution, which would address the second problem defined in Section 3.

<sup>1</sup>The manifold  $(\mathbb{S}^3)^n \times \mathbb{R}^{3n}$  can be expressed as a product of the manifolds  $\mathbb{S}^3$  ( $n$  times) and  $\mathbb{R}^{3n}$ . Therefore, its geodesic flow is the combination of the geodesic flows of individual manifolds. Since the geodesic flows in  $\mathbb{S}^{d-1}$  and  $\mathbb{R}^d$  are analytically available, so is the flow of the product manifold [26].

Recent studies have shown that SG-MCMC techniques [37, 38, 39, 40, 41] are closely related to optimization [42, 43, 44, 45, 28, 29] and they indeed have a strong potential in non-convex problems due to their randomized nature. In particular, it has been recently shown that, a simple variant of SG-MCMC is guaranteed to converge to a point near a local optimum in polynomial time [46, 47] and eventually converge to a point near the global optimum [43], even in non-convex settings. Even though these recent results illustrated the advantages of SG-MCMC in optimization, it is not clear how to develop an SG-MCMC-based optimization algorithm that can operate on manifolds. In this section, we will extend the SG-GMC algorithm in this vein to obtain a *parametric* algorithm, which is able to both sample from the posterior distribution and perform optimization for obtaining the MAP estimates depending on the choice of the practitioner. In other words, the algorithm should be able to address both problems that we defined in Section 3 with theoretical guarantees.

We start by defining a more compact notation that will facilitate the presentation of the algorithm. We define the variable  $\mathbf{x} \in \mathcal{X}$ , such that  $\mathbf{x} \triangleq [\mathbf{q}_1^\top, \dots, \mathbf{q}_n^\top, \mathbf{t}_1^\top, \dots, \mathbf{t}_n^\top]^\top$  and  $\mathcal{X} \triangleq (\mathbb{S}^3)^n \times \mathbb{R}^{3n}$ . The posterior density of interest then has the form  $\pi_{\mathcal{H}}(\mathbf{x}) \triangleq p(\mathbf{x}|\mathcal{D}) \propto \exp(-U(\mathbf{x}))$  with respect to the Hausdorff measure, where  $U$  is called the *potential energy* has the following form:  $U(\mathbf{x}) \triangleq -(\log p(\mathcal{D}|\mathbf{x}) + \log p(\mathbf{x})) = -(\log p(\mathcal{D}|\mathbf{Q}, \mathbf{T}) + \log p(\mathbf{Q}) + \log p(\mathbf{T}))$ . We define a *smooth embedding*  $\xi: \mathbb{R}^{6n} \mapsto \mathcal{X}$  such that  $\xi(\tilde{\mathbf{x}}) = \mathbf{x}$ . If we consider the embedded posterior density  $\pi_\lambda(\tilde{\mathbf{x}}) \triangleq p(\tilde{\mathbf{x}}|\mathcal{D})$  with respect to the Lebesgue measure, then by the area formula (cf. Theorem 1 in [48]), we have the following key property:  $\pi_{\mathcal{H}}(\mathbf{x}) = \pi_\lambda(\tilde{\mathbf{x}})/\sqrt{|\mathbf{G}(\tilde{\mathbf{x}})|}$ , where  $|\mathbf{G}|$  denotes the determinant of the Riemann metric tensor  $[\mathbf{G}(\tilde{\mathbf{x}})]_{i,j} \triangleq \sum_{l=1}^{7n} \frac{\partial x_l}{\partial \tilde{x}_i} \frac{\partial x_l}{\partial \tilde{x}_j}$  for all  $i, j \in \{1, \dots, 6n\}$ .

The main idea in our approach is to introduce an *inverse temperature* variable  $\beta \in \mathbb{R}_+$  and consider the *tempered* posterior distributions whose density is proportional to  $\exp(-\beta U(\mathbf{x}))$ . When  $\beta = 1$ , this density coincides with the original posterior; however, as  $\beta$  goes to infinity, the tempered density concentrates near the global minimum of the potential  $U$  [49, 50]. This important property implies that, for large enough  $\beta$ , a random sample that is drawn from the tempered posterior would be close to the global optimum and can therefore be used as a MAP estimate.

**Construction of the algorithm:** We will now construct the proposed algorithm. In particular, we will first extend the continuous-time Markov process proposed in [36] and develop a process whose marginal stationary distribution has a density proportional to  $\exp(-\beta U(\mathbf{x}))$  for any given  $\beta > 0$ . Then we will develop practical algorithms for generating samples from this tempered posterior.

We propose the following stochastic differential equation (SDE) in the Euclidean space by making use of the embedding  $\xi$ :

$$\begin{aligned} d\tilde{\mathbf{x}}_t &= \mathbf{G}(\tilde{\mathbf{x}}_t)^{-1} \mathbf{p}_t dt \\ d\mathbf{p}_t &= -\left( \nabla_{\tilde{\mathbf{x}}} U_\lambda(\tilde{\mathbf{x}}_t) + \frac{1}{2} \nabla_{\tilde{\mathbf{x}}} \log |\mathbf{G}| + c \mathbf{p}_t + \frac{1}{2} \nabla_{\tilde{\mathbf{x}}} (\mathbf{p}_t^\top \mathbf{G}^{-1} \mathbf{p}_t) \right) dt + \sqrt{\frac{2c}{\beta}} \mathbf{M}^\top \mathbf{M} dW_t, \end{aligned} \quad (8)$$

where  $\nabla_{\tilde{\mathbf{x}}} U_\lambda \triangleq -\nabla_{\tilde{\mathbf{x}}} \log \pi_\lambda$ ,  $\mathbf{G}$  and  $\mathbf{M}$  are short-hand notations for  $\mathbf{G}(\tilde{\mathbf{x}}_t)$  and  $[\mathbf{M}(\tilde{\mathbf{x}}_t)]_{ij} \triangleq \partial \mathbf{x}_i / \partial \tilde{\mathbf{x}}_j$ , respectively,  $\mathbf{p}_t \in \mathbb{R}^{6n}$  is called the *momentum* variable,  $c > 0$  is called the *friction*, and  $W_t$  denotes the standard Brownian motion in  $\mathbb{R}^{6n}$ .

We will first analyze the invariant measure of the SDE (8).

**Proposition 1.** *Let  $\varphi_t = [\tilde{\mathbf{x}}_t, \mathbf{p}_t^\top]^\top \in \mathbb{R}^{12n}$  and  $(\varphi_t)_{t \geq 0}$  be a Markov process that is a solution of the SDE (8). Then  $(\varphi_t)_{t \geq 0}$  has an invariant measure  $\mu_\varphi$ , whose density with respect to the Lebesgue measure is proportional to  $\exp(-\mathcal{E}_\lambda(\varphi))$ , where  $\mathcal{E}_\lambda$  is defined as follows:*

$$\mathcal{E}_\lambda(\varphi) \triangleq \beta U_\lambda(\tilde{\mathbf{x}}) + \frac{\beta}{2} \log |\mathbf{G}(\tilde{\mathbf{x}})| + \frac{\beta}{2} \mathbf{p}^\top \mathbf{G}(\tilde{\mathbf{x}})^{-1} \mathbf{p}. \quad (9)$$

All the proofs are given in the supplementary document. By using the area formula and the definitions of  $\mathbf{G}$  and  $\mathbf{M}$ , one can show that the density of  $\mu_\varphi$  can also be written with respect to the Hausdorff measure, as follows: (see Section 3.2 in [26] for details)  $\mathcal{E}_{\mathcal{H}}(\mathbf{x}, \mathbf{v}) \triangleq \beta U + \frac{\beta}{2} \mathbf{v}^\top \mathbf{v}$ , where  $\mathbf{v} = \mathbf{M}(\mathbf{M}^\top \mathbf{M})^{-1} \mathbf{p}$ . This result shows that, if we could exactly simulate the SDE (8), then the *marginal* distribution of the sample paths would converge to a measure  $\pi_{\mathcal{X}}$  on  $\mathcal{X}$  whose density is proportional to  $\exp(-\beta U(\mathbf{x}))$ . Therefore, for  $\beta = 1$  we would be sampling from  $\pi_{\mathcal{H}}$  (i.e. we recover SG-GMC), and for large  $\beta$ , we would be sampling near the global optimum of  $U$ . An illustration of the behavior of  $\beta$  on a toy example is provided in the supplementary material.

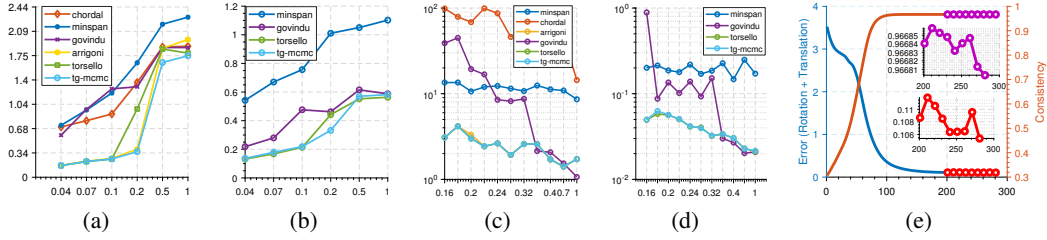


Figure 2: Synthetic Evaluations. **(a)** Mean Riemannian error vs noise variance. **(b)** Mean Euclidean (translational) error vs noise variance. **(c)** Riemannian error vs  $e$  for  $N = 50$ .  $e = |E|/N^2$  refers to graph completeness and  $N$  to the node count. **(d)** Euclidean error for  $N = 50$  vs  $e$ . **(e)** Monitoring the absolute error w.r.t. ground truth, during optimization and respective posterior sampling.

**Numerical integration:** We will now develop an algorithm for simulating (8) in discrete-time. We follow the approach given in [26, 36], where we split (8) into three disjoint parts and solve those parts analytically in an iterative fashion. The split SDE is given as follows:

$$A: \begin{cases} d\tilde{\mathbf{x}}_t = \mathbf{G}^{-1} \mathbf{p}_t dt \\ d\mathbf{p}_t = -\frac{1}{2} \nabla (\mathbf{p}_t^\top \mathbf{G}^{-1} \mathbf{p}_t) dt \end{cases} \quad B: \begin{cases} d\tilde{\mathbf{x}}_t = 0 \\ d\mathbf{p}_t = -c \mathbf{p}_t dt \end{cases} \quad O: \begin{cases} d\tilde{\mathbf{x}}_t = 0 \\ d\mathbf{p}_t = -(\nabla U_\lambda(\tilde{\mathbf{x}}_t) + \frac{1}{2} \nabla \log |\mathbf{G}|) dt \\ \quad + \sqrt{\frac{2c}{\beta}} \mathbf{M}^\top \mathbf{M} dW_t. \end{cases}$$

The nice property of these (stochastic) differential equations is that, each of them can be analytically simulated directly on the manifold  $\mathcal{X}$ , by using the identity  $\mathbf{x} = \xi(\tilde{\mathbf{x}})$  and the definitions of  $\mathbf{G}$ ,  $\mathbf{M}$ , and  $\mathbf{v}$ . In practice, one first needs to determine a sequence for the A, B, O steps, set a step-size  $h$  for integration along the time-axis  $t$ , and solve those steps one by one in an iterative fashion [51, 39]. In our applications, we have empirically observed that the sequence BOA provides better results among several other combinations, including the ABOBA scheme that was used in [36]. We provide the solutions of the A, B, O steps, as well as the required gradients in the supplementary material.

**Theoretical analysis:** In this section, we will provide non-asymptotic results for the proposed algorithm. Let us denote the output of the algorithm  $\{\mathbf{x}_k\}_{k=1}^N$ , where  $k$  denotes the iterations and  $N$  denotes the number of iterations. In the MAP estimation problem, we are interested in finding  $\mathbf{x}^* \triangleq \arg \min_{\mathbf{x}} U(\mathbf{x})$ , whereas for full Bayesian inference, we are interested in approximating posterior expectations with finite sample averages, i.e.  $\bar{\phi} \triangleq \int_{\mathcal{X}} \phi(\mathbf{x}) \pi_{\mathcal{H}}(\mathbf{x}) d\mathbf{x} \approx \hat{\phi} \triangleq (1/N) \sum_{k=1}^N \phi(\mathbf{x}_k)$ , where  $\phi$  is a test function.

As briefly discussed in [36], the convergence behavior of the SG-GMC algorithm can be directly analyzed within the theoretical framework presented in [39]. In a nutshell, the theory in [39] suggests that, with the BOA integration scheme, the bias  $|\mathbb{E}\hat{\phi} - \phi|$  is of order  $\mathcal{O}(N^{-1/2})$ .

In this study, we focus on the MAP estimation problem and analyze the *ergodic* error  $\mathbb{E}[\hat{U}_N - U^*]$ , where  $\hat{U}_N \triangleq (1/N) \sum_{k=1}^N U(\mathbf{x}_k)$  and  $U^* \triangleq U(\mathbf{x}^*)$ . This error resembles the bias where the test function  $\phi$  is chosen as the potential  $U$ ; however, on the contrary, it directly relates the sample average to the global optimum. Similar ergodic error notions have already been considered in non-convex optimization [52, 53, 28]. We present our main result in the following theorem. Due to space limitations and for avoiding obscuring the results, we present the required assumptions and the explicit forms of constants in the supplementary document.

**Theorem 1.** *Assume that the conditions given in the supp. doc. hold. If the iterates are obtained by using the BOA the scheme, then the following bound holds for  $\beta$  small enough and  $\mathcal{X} = (\mathbb{S}^3)^n \times \mathbb{R}^{3n}$ .*

$$|\mathbb{E}\hat{U}_N - U^*| = \mathcal{O}(\beta/(Nh) + h/\beta + 1/\beta), \quad (10)$$

*Sketch of the proof.* We decompose the error into two terms:  $\mathbb{E}[\hat{U}_N - U^*] = \mathcal{A}_1 + \mathcal{A}_2$ , where  $\mathcal{A}_1 \triangleq \mathbb{E}[\hat{U}_N - \bar{U}_\beta]$  and  $\mathcal{A}_2 \triangleq [\bar{U}_\beta - U^*] \geq 0$ , and  $\bar{U}_\beta \triangleq \int_{\mathcal{X}} U(\mathbf{x}) \pi_{\mathbf{x}}(d\mathbf{x})$ . The term  $\mathcal{A}_1$  is the bias term, which can be bounded by using existing results. The rest of the proof deals with bounding  $\mathcal{A}_2$ , where we incorporate ideas from [43]. The full proof resides in the supplementary.  $\square$

Table 1: Evaluations on EPFL Benchmark.

|               | Ozyesil et. al. |       | R-GODEC |       | Govindu |       | Torsello |       | EIG-SE(3) |       | TG-MCMC      |              |
|---------------|-----------------|-------|---------|-------|---------|-------|----------|-------|-----------|-------|--------------|--------------|
|               | MRE             | MTE   | MRE     | MTE   | MRE     | MTE   | MRE      | MTE   | MRE       | MTE   | MRE          | MTE          |
| HerzJesus-P8  | 0.060           | 0.007 | 0.040   | 0.009 | 0.106   | 0.015 | 0.106    | 0.015 | 0.040     | 0.004 | 0.106        | 0.015        |
| HerzJesus-P25 | 0.140           | 0.065 | 0.130   | 0.038 | 0.081   | 0.020 | 0.081    | 0.020 | 0.070     | 0.010 | 0.081        | 0.020        |
| Fountain-P11  | 0.030           | 0.004 | 0.030   | 0.006 | 0.071   | 0.004 | 0.071    | 0.004 | 0.030     | 0.004 | 0.071        | 0.004        |
| Entry-P10     | 0.560           | 0.203 | 0.440   | 0.433 | 0.101   | 0.035 | 0.101    | 0.035 | 0.040     | 0.009 | 0.090        | 0.035        |
| Castle-P19    | 3.690           | 1.769 | 1.570   | 1.493 | 0.393   | 0.147 | 0.393    | 0.147 | 1.480     | 0.709 | 0.393        | 0.148        |
| Castle-P30    | 1.970           | 1.393 | 0.780   | 1.123 | 0.631   | 0.323 | 0.629    | 0.321 | 0.530     | 0.212 | 0.622        | 0.285        |
| Average       | 1.075           | 0.574 | 0.498   | 0.517 | 0.230   | 0.091 | 0.230    | 0.090 | 0.365     | 0.158 | <b>0.227</b> | <b>0.085</b> |

Theorem 1 shows that the proposed algorithm will eventually provide samples that are close to the global optimizer  $\mathbf{x}^*$  even when  $U$  is non-convex. This result is fundamentally different from the guarantees for the existing convex optimization algorithms on manifolds [54, 55], and is mainly due to the stochasticity of the algorithm that is introduced by the Brownian motion. However, despite this nice theoretical property, in practice our algorithm will still be affected by the *meta-stability phenomenon*, where it will converge near a local minimum and stay there for an exponential amount of time [47].

We also note that our proof covers only the case where  $\mathcal{X} = (\mathbb{S}^3)^n \times \mathbb{R}^{3n}$ ; however, we believe that it can be easily extended to more general setting. We also note that our gradient computations can be replaced with stochastic gradients in the case of large-scale applications where the number of data points can be prohibitively large, so that computing the gradients at each iteration becomes practically infeasible. The same theoretical results hold as long as the stochastic gradients are unbiased.

## 5 Experiments

In a sequel of evaluations, we will be benchmarking our TG-MCMC against the state of the art methods including subsets of: convex programming of Ozyesil et. al. [56], Lie algebraic method of Govindu [15], dual quaternions linearization of Torsello et. al. [15], direct EIG-SE3 method of Arrigoni [12] and R-GODEC [57]. We also include two baseline methods: 1. propagating the pose information along one possible minimum spanning tree, 2. the chordal averaging [58].

**Synthetic Evaluations:** We first synthesize random problems by drawing quaternions from Bingham and translations from Gaussian distributions, and randomly dropping  $(100|E|/N^2)\%$  edges from a fully connected pose graph. On these problems, we run a series of tests including monitoring the gradient steps, noise robustness, tolerance to graph completeness (sparsity) and fidelity w.r.t. ground truth. For each test, we distort the graph for the entity we test, i.e. add noise on nodes if we test the noise resilience. The rotational errors are evaluated by the true Riemannian distance,  $\|\log(\mathbf{R}^T \hat{\mathbf{R}})\|$ , the translations by Euclidean [59]. Fig. 2 plots our findings. It is noticeable that our accuracy is always on par with or better than the state of the art for moderate problems. In presence of increased noise (Figures 2(a), 2(b)) or sparsified graph structure leading to missing data (Figures 2(c), 2(d)), our method shows clear advantage in both rotational and translational components of the error. This is thanks to our probabilistic formulation and theoretically grounded inference scheme.

**Results in Real Data:** We now evaluate our framework by running SFM on the EPFL Benchmark [60], that provide 8 to 30 images per dataset, along with ground-truth camera transformations. Similar to [12], we use the ground truth scale to circumvent its ambiguity. The mean rotation and translation errors (MRE, MTE) are depicted in Tab. 1. Notice that when rotations and translations are combined, our optimization results in superior minimum for both, not to mention the uncertainty information computed as a by-product. While many methods can perform similarly on easy sets, a clear advantage is visible on Castle sequences where severe noise and missing connections are present. There, for instance, EIG-SE(3) also fails to find a good closed form solution.

Next, we qualitatively demonstrate the unique capability of our method, uncertainty estimation on various SFM problems and datasets [61, 62, 60]. To do so, we first run our optimizer setting  $\beta$  to infinity<sup>2</sup> for  $> 400$  iterations. After that point, depending on the dataset, we set  $\beta$  to a smaller value

<sup>2</sup>Note that the case  $\beta \rightarrow \infty$  renders the SDE degenerate and hence, cannot be analyzed by using our tools. However, due to meta-stability, the algorithm performs similarly either for large  $\beta$  or for  $\beta \rightarrow \infty$ .



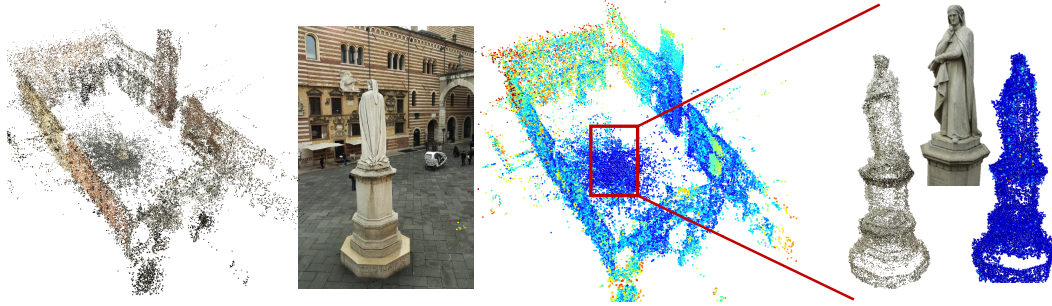


Figure 3: Uncertainty estimation in the Dante Square. From left to right: the colored reconstruction (bundle adjustment used in 3D structure only), a sample image from the dataset, reconstructed points colored w.r.t. uncertainty value, a close-up to the center of the square, Dante statue.

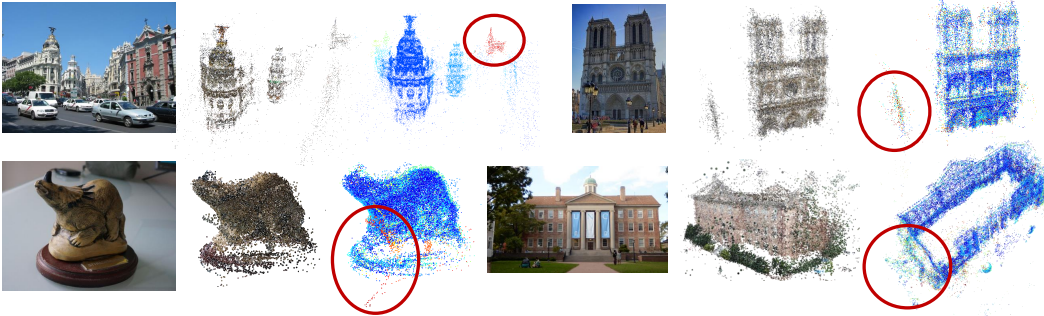


Figure 4: Visualization of uncertainty in Notre Dame, Angel, Dinosaurs and Fountain datasets.

( $\sim 1000$ ), allowing the sampling of posterior for 40 times. This behaviour is shown in Fig. 2(e). For each sample, that is a solution of the problem in Eq. 1, we perform a 3D reconstruction, similar to [16]: We first estimate 2D keypoints and relative rotations by running 1) VSFM [63] 2) two-frame bundle adjustment [64, 65] (BA) on image pairs, resulting in pairwise poses, as well as a rough two-view 3D structure. We run our method on these relative poses, computing the absolute estimates. Fixing the estimated poses, a second BA then optimizes for the optimal 3D structure. At the end, we obtain 40 3D scenes per dataset. For each point of each scene, we record the mean and variance across different reconstructions, transferring the uncertainty estimation to the 3D cloud of points. In Figures 3 and 4, we colorize each point by mapping the uncertainty value to RGB space using a jet-colormap, with a scale proportional to the diameter of reconstruction. It is consistently visible that our uncertainty estimates could capture regions of space where there are more and reliable data: Outlying points, noise or distant structures can be identified by interpreting the uncertainty.

## 6 Conclusion

We have proposed TG-MCMC, a manifold-aware, tempered rigid motion synchronization algorithm with a novel probabilistic formulation. TG-MCMC enjoys unique properties of trading-off approximately globally optimal solutions with non-asymptotic guarantees, to drawing samples from the posterior distribution, providing uncertainty estimates for the PGO-initialization problem.

Our algorithm paves the way to a diverse potential future research: First, stochastic gradients can be employed to handle large problems, scaling up to hundreds of thousands of nodes. Next, the uncertainty estimates can be plugged into existing pipelines such as BA or PGO to further improve their quality. We also leave it as a future work to investigate different simulation schemes by altering the order of and combining differently the A, B, and O steps. Finally, TG-MCMC can be extended to different problems, still maintaining its nice theoretical properties.



## Acknowledgements

We would like to thank Robert M. Gower and François Portier for fruitful discussions and Hans Peschke for his feedback and efforts in verifying the correctness of our descriptions. We thank Antonio Vargas of the Mathematics-StackExchange for providing the reference on inequalities for generalized hypergeometric functions. This work is partly supported by the French National Research Agency (ANR) as a part of the FBIMATRIX project (ANR-16-CE23-0014) and by the industrial chair Machine Learning for Big Data from Télécom ParisTech.

## References

- [1] Arno Knapitsch, Jaesik Park, Qian-Yi Zhou, and Vladlen Koltun. Tanks and temples: Benchmarking large-scale scene reconstruction. *ACM Transactions on Graphics (TOG)*, 36(4):78, 2017.
- [2] Luca Carlone and Giuseppe Carlo Calafiore. Convex relaxations for pose graph optimization with outliers. *IEEE Robotics and Automation Letters*, 3:1160–1167, 2018.
- [3] Bill Triggs, Philip F McLauchlan, Richard I Hartley, and Andrew W Fitzgibbon. Bundle adjustment—a modern synthesis. In *International workshop on vision algorithms*, pages 298–372. Springer, 1999.
- [4] Tolga Birdal and Slobodan Ilic. Cad priors for accurate and flexible instance reconstruction. In *The IEEE International Conference on Computer Vision (ICCV)*, Oct 2017.
- [5] Daniel F Huber and Martial Hebert. Fully automatic registration of multiple 3d data sets. *Image and Vision Computing*, 21(7):637–650, 2003.
- [6] Tolga Birdal, Emrah Bala, Tolga Eren, and Slobodan Ilic. Online inspection of 3d parts via a locally overlapping camera network. In *Applications of Computer Vision (WACV), 2016 IEEE Winter Conference on*, pages 1–10. IEEE, 2016.
- [7] Rainer Kümmerle, Giorgio Grisetti, Hauke Strasdat, Kurt Konolige, and Wolfram Burgard. g2o: A general framework for graph optimization. In *Robotics and Automation (ICRA), 2011 IEEE International Conference on*, pages 3607–3613. IEEE, 2011.
- [8] Venu Madhav Govindu. Combining two-view constraints for motion estimation. In *Computer Vision and Pattern Recognition, 2001. CVPR 2001. Proceedings of the 2001 IEEE Computer Society Conference on*, volume 2, pages II–II. IEEE, 2001.
- [9] Luca Carlone, Roberto Tron, Kostas Daniilidis, and Frank Dellaert. Initialization techniques for 3d slam: a survey on rotation estimation and its use in pose graph optimization. In *Robotics and Automation (ICRA), 2015 IEEE International Conference on*, pages 4597–4604. IEEE, 2015.
- [10] Roberto Tron, Xiaowei Zhou, and Kostas Daniilidis. A survey on rotation optimization in structure from motion. In *Proceedings of the IEEE Conference on Computer Vision and Pattern Recognition Workshops*, pages 77–85, 2016.
- [11] Johan Fredriksson and Carl Olsson. Simultaneous multiple rotation averaging using lagrangian duality. In *Asian Conference on Computer Vision*, pages 245–258. Springer, 2012.
- [12] Federica Arrigoni, Andrea Fusiello, and Beatrice Rossi. Spectral motion synchronization in se (3). *arXiv preprint arXiv:1506.08765*, 2015.
- [13] Federica Arrigoni, Andrea Fusiello, and Beatrice Rossi. Camera motion from group synchronization. In *3D Vision (3DV), 2016 Fourth International Conference on*, pages 546–555. IEEE, 2016.
- [14] Andrea Torsello, Emanuele Rodola, and Andrea Albarelli. Multiview registration via graph diffusion of dual quaternions. In *Computer Vision and Pattern Recognition (CVPR), 2011 IEEE Conference on*, pages 2441–2448. IEEE, 2011.

- [15] Venu Madhav Govindu. Lie-algebraic averaging for globally consistent motion estimation. In *Computer Vision and Pattern Recognition, 2004. CVPR 2004. Proceedings of the 2004 IEEE Computer Society Conference on*, volume 1, pages I–I. IEEE, 2004.
- [16] Avishek Chatterjee and Venu Madhav Govindu. Efficient and robust large-scale rotation averaging. In *Computer Vision (ICCV), 2013 IEEE International Conference on*, pages 521–528. IEEE, 2013.
- [17] Richard Hartley, Khurram Aftab, and Jochen Trumpf. L1 rotation averaging using the weiszfeld algorithm. In *Computer Vision and Pattern Recognition (CVPR), 2011 IEEE Conference on*, pages 3041–3048. IEEE, 2011.
- [18] Avishek Chatterjee and Venu Madhav Govindu. Robust relative rotation averaging. *IEEE transactions on pattern analysis and machine intelligence*, 40(4):958–972, 2018.
- [19] Kyle Wilson, David Bindel, and Noah Snavely. When is rotations averaging hard? In *European Conference on Computer Vision*, pages 255–270. Springer, 2016.
- [20] D.M. Rosen, L. Carlone, A.S. Bandeira, and J.J. Leonard. SE-Sync: A certifiably correct algorithm for synchronization over the special Euclidean group. Technical Report MIT-CSAIL-TR-2017-002, Computer Science and Artificial Intelligence Laboratory, Massachusetts Institute of Technology, Cambridge, MA, February 2017.
- [21] Jesus Briales and Javier Gonzalez-Jimenez. Fast global optimality verification in 3d slam. In *Intelligent Robots and Systems (IROS), 2016 IEEE/RSJ International Conference on*, pages 4630–4636. IEEE, 2016.
- [22] Anders Eriksson, Carl Olsson, Fredrik Kahl, and Tat-Jun Chin. Rotation averaging and strong duality. In *The IEEE Conference on Computer Vision and Pattern Recognition (CVPR)*, June 2018.
- [23] Jesus Briales and Javier Gonzalez-Jimenez. Initialization of 3d pose graph optimization using lagrangian duality. In *Robotics and Automation (ICRA), 2017 IEEE International Conference on*, pages 5134–5139. IEEE, 2017.
- [24] Roberto Tron and Kostas Daniilidis. Statistical pose averaging with non-isotropic and incomplete relative measurements. In *European Conference on Computer Vision*, pages 804–819. Springer, 2014.
- [25] Christopher Bingham. An antipodally symmetric distribution on the sphere. *The Annals of Statistics*, pages 1201–1225, 1974.
- [26] Simon Byrne and Mark Girolami. Geodesic monte carlo on embedded manifolds. *Scandinavian Journal of Statistics*, 40(4):825–845, 2013.
- [27] R. M. Neal. MCMC using Hamiltonian dynamics. *Handbook of Markov Chain Monte Carlo*, 2(11):2, 2011.
- [28] Umut Simsekli, Cagatay Yildiz, Thanh Huy Nguyen, Ali Taylan Cemgil, and Gaël Richard. Asynchronous stochastic quasi-Newton MCMC for non-convex optimization. In *ICML 2018*, 2018.
- [29] X. Gao, M. Gürbüzbalaban, and L. Zhu. Global convergence of stochastic gradient Hamiltonian Monte Carlo for non-convex stochastic optimization: Non-asymptotic performance bounds and momentum-based acceleration. *arXiv preprint arXiv:1809.04618*, 2018.
- [30] Vincent Lepetit, Pascal Fua, et al. Monocular model-based 3d tracking of rigid objects: A survey. *Foundations and Trends® in Computer Graphics and Vision*, 1(1):1–89, 2005.
- [31] Benjamin Busam, Tolga Birdal, and Nassir Navab. Camera pose filtering with local regression geodesics on the riemannian manifold of dual quaternions. In *IEEE International Conference on Computer Vision Workshop (ICCVW)*, October 2017.

- [32] Jared Glover, Gary Bradski, and Radu Bogdan Rusu. Monte carlo pose estimation with quaternion kernels and the bingham distribution. In *Robotics: science and systems*, volume 7, page 97, 2012.
- [33] Gerhard Kurz, Igor Gilitschenski, Simon Julier, and Uwe D Hanebeck. Recursive estimation of orientation based on the bingham distribution. In *Information Fusion (FUSION), 2013 16th International Conference on*, pages 1487–1494. IEEE, 2013.
- [34] J. Glover and L. P. Kaelbling. Tracking the spin on a ping pong ball with the quaternion bingham filter. In *2014 IEEE International Conference on Robotics and Automation (ICRA)*, pages 4133–4140, May 2014.
- [35] Norman Earl Steenrod. *The topology of fibre bundles*, volume 14. Princeton University Press, 1951.
- [36] Chang Liu, Jun Zhu, and Yang Song. Stochastic gradient geodesic mcmc methods. In *Advances in Neural Information Processing Systems*, pages 3009–3017, 2016.
- [37] M. Welling and Y. W. Teh. Bayesian learning via stochastic gradient Langevin dynamics. In *Proceedings of the 28th International Conference on Machine Learning (ICML-11)*, pages 681–688, 2011.
- [38] Y. A. Ma, T. Chen, and E. Fox. A complete recipe for stochastic gradient MCMC. In *Advances in Neural Information Processing Systems*, pages 2899–2907, 2015.
- [39] C. Chen, N. Ding, and L. Carin. On the convergence of stochastic gradient MCMC algorithms with high-order integrators. In *Advances in Neural Information Processing Systems*, pages 2269–2277, 2015.
- [40] A. Durmus, U. Simsekli, E. Moulines, R. Badeau, and G. Richard. Stochastic gradient Richardson-Romberg Markov Chain Monte Carlo. In *Advances in Neural Information Processing Systems*, pages 2047–2055, 2016.
- [41] Umut Simsekli. Fractional Langevin Monte Carlo: Exploring Lévy driven stochastic differential equations for Markov Chain Monte Carlo. In *International Conference on Machine Learning*, 2017.
- [42] Arnak S Dalalyan. Further and stronger analogy between sampling and optimization: Langevin monte carlo and gradient descent. *arXiv preprint arXiv:1704.04752*, 2017.
- [43] M. Raginsky, A. Rakhlin, and M. Telgarsky. Non-convex learning via stochastic gradient Langevin dynamics: a nonasymptotic analysis. In *Proceedings of the 2017 Conference on Learning Theory*, volume 65, pages 1674–1703, 2017.
- [44] U. Simsekli, R. Badeau, T. Cemgil, and G. Richard. Stochastic quasi-Newton Langevin Monte Carlo. In *International Conference on Machine Learning*, pages 642–651, 2016.
- [45] N. Ye and Z. Zhu. Stochastic fractional Hamiltonian Monte Carlo. In *International Joint Conference on Artificial Intelligence, IJCAI-18*, pages 3019–3025. International Joint Conferences on Artificial Intelligence Organization, 7 2018.
- [46] Y. Zhang, P. Liang, and M. Charikar. A hitting time analysis of stochastic gradient langevin dynamics. In *Proceedings of the 2017 Conference on Learning Theory*, volume 65, pages 1980–2022, 2017.
- [47] Belinda Tzen, Tengyuan Liang, and Maxim Raginsky. Local optimality and generalization guarantees for the langevin algorithm via empirical metastability. In *Conference on Learning Theory*, 2018.
- [48] Persi Diaconis, Susan Holmes, Mehrdad Shahshahani, et al. Sampling from a manifold. In *Advances in Modern Statistical Theory and Applications: A Festschrift in honor of Morris L. Eaton*, pages 102–125. Institute of Mathematical Statistics, 2013.
- [49] C. Hwang. Laplace’s method revisited: weak convergence of probability measures. *The Annals of Probability*, pages 1177–1182, 1980.

- [50] S. B. Gelfand and S. K. Mitter. Recursive stochastic algorithms for global optimization in  $\mathbb{R}^d$ . *SIAM Journal on Control and Optimization*, 29(5):999–1018, 1991.
- [51] Ben Leimkuhler and Charles Matthews. *Molecular Dynamics: With Deterministic and Stochastic Numerical Methods*, volume 39. Springer, 2015.
- [52] X. Lian, Y. Huang, Y. Li, and J. Liu. Asynchronous parallel stochastic gradient for nonconvex optimization. In *Advances in Neural Information Processing Systems*, pages 2737–2745, 2015.
- [53] C. Chen, D. Carlson, Z. Gan, C. Li, and L. Carin. Bridging the gap between stochastic gradient MCMC and stochastic optimization. In *AISTATS*, 2016.
- [54] H. Zhang and S. Sra. First-order methods for geodesically convex optimization. In *Conference on Learning Theory*, pages 1617–1638, 2016.
- [55] Y. Liu, F. Shang, J. Cheng, H. Cheng, and L. Jiao. Accelerated first-order methods for geodesically convex optimization on Riemannian manifolds. In *Advances in Neural Information Processing Systems*, pages 4875–4884, 2017.
- [56] Onur Özyeşil, Amit Singer, and Ronen Basri. Stable camera motion estimation using convex programming. *SIAM Journal on Imaging Sciences*, 8(2):1220–1262, 2015.
- [57] Federica Arrigoni, Luca Magri, Beatrice Rossi, Pasqualina Fragneto, and Andrea Fusiello. Robust absolute rotation estimation via low-rank and sparse matrix decomposition. In *3D Vision (3DV), 2014 2nd International Conference on*, volume 1, pages 491–498. IEEE, 2014.
- [58] Richard Hartley, Jochen Trunpf, Yuchao Dai, and Hongdong Li. Rotation averaging. *International journal of computer vision*, 103(3):267–305, 2013.
- [59] Adrian Haarbach, Tolga Birdal, and Slobodan Ilic. Survey of higher order rigid body motion interpolation methods for keyframe animation and continuous-time trajectory estimation. In *3D Vision (3DV), 2018 Sixth International Conference on*, pages 381–389. IEEE, 2018.
- [60] Christoph Strecha, Wolfgang Von Hansen, Luc Van Gool, Pascal Fua, and Ulrich Thoennessen. On benchmarking camera calibration and multi-view stereo for high resolution imagery. In *Computer Vision and Pattern Recognition, 2008. CVPR 2008. IEEE Conference on*, pages 1–8. Ieee, 2008.
- [61] 3df zephyr reconstruction showcase. <https://www.3dflow.net/3df-zephyr-reconstruction-showcase/>, 2018. Accessed: 2018-05-15.
- [62] Kyle Wilson and Noah Snavely. Robust global translations with ldsfm. In *Proceedings of the European Conference on Computer Vision (ECCV)*, 2014.
- [63] Changchang Wu et al. Visualsfm: A visual structure from motion system. *online*, 2011.
- [64] Tolga Birdal, Ievgeniia Dobryden, and Slobodan Ilic. X-tag: A fiducial tag for flexible and accurate bundle adjustment. In *IEEE International Conference on 3D Vision*, October 2016.
- [65] Sameer Agarwal, Keir Mierle, and Others. Ceres solver. <http://ceres-solver.org>, 2018.
- [66] Richard M Murray. *A mathematical introduction to robotic manipulation*. CRC press, 1994.
- [67] A Morawiec and DP Field. Rodrigues parameterization for orientation and misorientation distributions. *Philosophical Magazine A*, 73(4):1113–1130, 1996.
- [68] F Sebastian Grassia. Practical parameterization of rotations using the exponential map. *Journal of graphics tools*, 3(3):29–48, 1998.
- [69] K. V Mardia and P. E Jupp. *Directional statistics*, volume 494. John Wiley & Sons, 2009.
- [70] Yudell L Luke. Inequalities for generalized hypergeometric functions. *Journal of Approximation Theory*, 5(1):41–65, 1972.
- [71] Y. Nesterov. *Introductory lectures on convex optimization: A basic course*, volume 87. Springer Science & Business Media, 2013.

- [72] F. Dai and Y. Xu. *Approximation theory and harmonic analysis on spheres and balls*. Springer, 2013.
- [73] Alfred Kume and Andrew TA Wood. On the derivatives of the normalising constant of the bingham distribution. *Statistics & probability letters*, 77(8):832–837, 2007.
- [74] Joan Sola. Quaternion kinematics for the error-state kalman filter. *arXiv preprint arXiv:1711.02508*, 2017.
- [75] Johannes Lutz Schönberger and Jan-Michael Frahm. Structure-from-motion revisited. In *Conference on Computer Vision and Pattern Recognition (CVPR)*, 2016.
- [76] Johannes Lutz Schönberger, Enliang Zheng, Marc Pollefeys, and Jan-Michael Frahm. Pixelwise view selection for unstructured multi-view stereo. In *European Conference on Computer Vision (ECCV)*, 2016.

## Appendix

### A Comparison to exponential coordinates

Many optimization algorithms tend to favor Rodrigues vector (exponential coordinates) [66] parameterization due to  $R^3$  embedding and geodesics being straight lines [67]. This also leads to simpler Jacobian forms. In this paper, we argue that unit quaternions are more suitable for the approach we pursue: First, 3-vector formulations suffer from infinitely many singularities when the rotation angle approaches 0,  $\|\mathbf{a}\| \rightarrow 0$ , whereas quaternions avoid them [68]. Moreover, quaternions have single redundancy in the representation  $\mathbf{q} = -\mathbf{q}$ , whereas the normed vectors possess infinite redundancy, i.e. the norm can grow indefinitely, but the angle lies in range  $[0 - 2\pi]$ . These make it harder to define continuous distributions directly on Rodrigues vectors. Yet, for quaternions there exists the natural antipodally symmetric Bingham distributions.

### B Illustration of tempered posteriors

In this study we consider the *tempered* posterior distributions whose density is controlled by the inverse temperature variable  $\beta$ . When  $\beta = 1$ , the posterior density coincides with the original posterior; however, as  $\beta$  goes to infinity, the tempered density concentrates near the global minimum of the potential  $U$  [49, 50]. As we mentioned in the main document, this important property implies that, for large enough  $\beta$ , a random sample that is drawn from the tempered posterior would be close to the global optimum and can therefore be used as a MAP estimate.

The figure below illustrates this phenomenon on a simple 2-component Gaussian mixture: when  $\beta = 1$  we can observe that both modes are visible, but when  $\beta = 20$  the mode on the right vanishes and the distribution concentrates around the global mode.

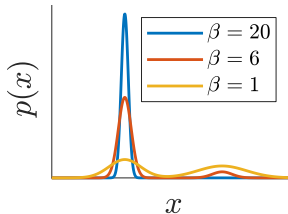


Figure 5: Illustration of tempered posteriors on a simple Gaussian mixture model.

### C Numerical Integration

In this section, we provide the details of the numerical integration scheme that was explained in Section 4 of the main document. In short, the overall scheme is an extension of [36], where we introduce the inverse temperature  $\beta$ .

Once the gradients with respect to the latent variables are computed, i.e.:

$$\nabla_{\mathbf{x}} U(\mathbf{x}) \equiv \{\nabla_{\mathbf{q}_1} U(\mathbf{x}), \dots, \nabla_{\mathbf{q}_n} U(\mathbf{x}), \nabla_{\mathbf{t}_1} U(\mathbf{x}), \dots, \nabla_{\mathbf{t}_n} U(\mathbf{x})\}, \quad (11)$$

we can update each of the variables  $\mathbf{q}_1, \dots, \mathbf{q}_n, \mathbf{t}_1, \dots, \mathbf{t}_n$  independently from each other, meaning that, the split integration steps, A, B, O can be applied to each of these variables independently. The operations A, B, O will differ depending on the manifold of the particular variable, therefore we will define these operations both on  $\mathbb{S}^3$  and  $\mathbb{R}^3$  for the two sets of variables  $\{\mathbf{q}_i\}_{i=1}^n$  and  $\{\mathbf{t}_i\}_{i=1}^n$ , respectively.

As we split  $\mathbf{x}$  into  $\{\mathbf{q}_i\}_{i=1}^n$  and  $\{\mathbf{t}_i\}_{i=1}^n$ , we similarly split the variable  $\mathbf{v}$  into  $\{\mathbf{v}_i^{\mathbf{q}}\}_{i=1}^n$  and  $\{\mathbf{v}_i^{\mathbf{t}}\}_{i=1}^n$  in order to facilitate the presentation.

#### C.1 Update equations for the rotation components

Set a step-size  $h$ . For each  $\{\mathbf{q}_i, \mathbf{v}_i^{\mathbf{q}}\}$  pairs, the operations A, B, O have the following analytical form:

**Step A:**

Set  $\alpha = \|\mathbf{v}_i^{\mathbf{q}}\|$ ,  $\mathbf{q}' \leftarrow \mathbf{q}_i$  and  $\mathbf{v}' \leftarrow \mathbf{v}_i^{\mathbf{q}}$ .

$$\mathbf{q}_i \leftarrow \mathbf{q}' \cos(\alpha h) + (\mathbf{v}'/\alpha) \sin(\alpha h) \quad (12)$$

$$\mathbf{v}_i^{\mathbf{q}} \leftarrow -\alpha \mathbf{q}' \sin(\alpha h) + \mathbf{v}' \cos(\alpha h) \quad (13)$$

**Step B:**

$$\mathbf{v}_i^{\mathbf{q}} \leftarrow \exp(-ch) \mathbf{v}_i^{\mathbf{q}} \quad (14)$$

**Step O:**

Set  $\mathbf{v}' \leftarrow \mathbf{v}_i^{\mathbf{q}}$  and  $\mathbf{g} \leftarrow \nabla_{\mathbf{q}_i} U(\mathbf{x})$

$$\mathbf{v}_i^{\mathbf{q}} \leftarrow \mathbf{v}' + P(\mathbf{q}_i)(-h\mathbf{g} + \sqrt{2c/\beta} \mathbf{z}_i^{\mathbf{q}}), \quad (15)$$

where  $P(\mathbf{q}) = (\mathbf{I} - \mathbf{q}\mathbf{q}^\top)$  denotes the projector and  $\mathbf{z}_i^{\mathbf{q}}$  denotes a standard Gaussian random variable on  $\mathbb{R}^4$ .

## C.2 Update equations for the translation components

Set a step-size  $h$ . For each  $\{\mathbf{t}_i, \mathbf{v}_i^{\mathbf{t}}\}$  pairs, the operations A, B, O have the following analytical form:

**Step A:**

$$\mathbf{t}_i \leftarrow \mathbf{t}_i + h\mathbf{v}_i^{\mathbf{t}} \quad (16)$$

**Step B:**

$$\mathbf{v}_i^{\mathbf{t}} \leftarrow \exp(-ch) \mathbf{v}_i^{\mathbf{t}} \quad (17)$$

**Step O:**

Set  $\mathbf{v}' \leftarrow \mathbf{v}_i^{\mathbf{t}}$  and  $\mathbf{g} \leftarrow \nabla_{\mathbf{t}_i} U(\mathbf{x})$

$$\mathbf{v}_i^{\mathbf{t}} \leftarrow \mathbf{v}' + (-h\mathbf{g} + \sqrt{2c/\beta} \mathbf{z}_i^{\mathbf{t}}), \quad (18)$$

where  $\mathbf{z}_i^{\mathbf{t}}$  denotes a standard Gaussian random variable on  $\mathbb{R}^3$ .

## C.3 Algorithm pseudocode

We illustrate the overall algorithm in Algorithm 1

---

### Algorithm 1: TG-MCMC

---

```

1 input:  $\mathbf{x}_0 = \{\mathbf{q}_1, \dots, \mathbf{q}_n, \mathbf{t}_1, \dots, \mathbf{t}_n\}$ ,  $\mathbf{v} = \{\mathbf{v}_1^{\mathbf{q}}, \dots, \mathbf{v}_n^{\mathbf{q}}, \mathbf{v}_1^{\mathbf{t}}, \dots, \mathbf{v}_n^{\mathbf{t}}\}$ ,  $\beta, c, h$ 
2 for  $i = 1, \dots, N$  do
3   Compute the gradient  $\nabla_{\mathbf{x}} U(\mathbf{x}_i)$ 
4   // Update the rotation components
5   for  $j = 1, \dots, n$  do
6     Run the B, O, A steps (in this order) on  $\mathbf{q}_j, \mathbf{v}_j^{\mathbf{q}}$  (Section C.1)
7     // Update the translation components
8     for  $j = 1, \dots, n$  do
9       Run the B, O, A steps (in this order) on  $\mathbf{t}_j, \mathbf{v}_j^{\mathbf{t}}$  (Section C.2)

```

---

## D Assumptions

In this section, we state the assumptions that imply our theoretical results.

**H1.** *The gradient of the potential is Lipschitz continuous, i.e. there exists  $L < \infty$ , such that  $\|\nabla_{\mathbf{x}} U(\mathbf{x}) - \nabla_{\mathbf{x}} U(\mathbf{x}')\| \leq L d_{\mathcal{X}}(\mathbf{x}, \mathbf{x}')$ ,  $\forall \mathbf{x}, \mathbf{x}' \in \mathcal{X}$ , where  $d_{\mathcal{X}}$  denotes the geodesic distance on  $\mathcal{X}$ .*

**H2.** *The second-order moments of  $\pi_{\mathbf{x}}$  are bounded and satisfies the following inequality:  $\int_{\mathcal{X}} \|\mathbf{x}\|^2 \pi_{\mathbf{x}}(d\mathbf{x}) \leq \frac{C}{\beta}$ , for some  $C > 0$ .*



**H3.** Let  $\psi$  be a functional that is the unique solution of a Poisson equation that is defined as follows:

$$\mathcal{L}_n \psi(\varphi_n) = U(\mathbf{x}_n) - \bar{U}_\beta, \quad (19)$$

where  $\varphi_n = [\tilde{\mathbf{x}}_n^\top, \mathbf{p}_n^\top]^\top$ ,  $\mathcal{L}_n$  is the generator of (8) at  $t = nh$  (see [39] for the definition). The functional  $\psi$  and its up to third-order derivatives  $\mathcal{D}^k \psi$  are bounded by a function  $V(\varphi)$ , such that  $\|\mathcal{D}^k \psi\| \leq C_k V^{r_k}$  for  $k = 0, 1, 2, 3$  and  $C_k, r_k > 0$ . Furthermore,  $\sup_n \mathbb{E} V^r(\mathbf{x}_n) < \infty$  and  $V$  is smooth such that  $\sup_{s \in (0,1)} V^r(s\varphi + (1-s)\varphi') \leq C(V^r(\varphi) + V^r(\varphi'))$  for all  $\varphi, \varphi' \in \mathbb{R}^{12n}$ ,  $r \leq \max 2r_k$ , and  $C > 0$ .

## E Proof of Proposition 1

*Sketch of the proof.* We start by rewriting the SDE given in (8) as follows:

$$d\varphi_t = \left\{ - \left( \underbrace{\begin{bmatrix} 0 & 0 \\ 0 & \frac{e\mathbf{M}^\top \mathbf{M} \mathbf{I}}{\beta} \end{bmatrix}}_{\mathbf{D}} + \underbrace{\begin{bmatrix} 0 & -\frac{\mathbf{I}}{\beta} \\ \frac{\mathbf{I}}{\beta} & 0 \end{bmatrix}}_{\mathbf{Q}} \right) \underbrace{\begin{bmatrix} \mathcal{A}(\tilde{\mathbf{x}}_t, \mathbf{p}_t, \beta) \\ \beta \mathbf{G}^{-1} \mathbf{p}_t \end{bmatrix}}_{\nabla_{\varphi} \mathcal{E}_\lambda(\varphi_t)} \right\} dt + \sqrt{2\mathbf{D}} dW_t. \quad (20)$$

where  $\mathcal{A}(\tilde{\mathbf{x}}_t, \mathbf{p}_t, \beta) \triangleq \beta \nabla_{\tilde{\mathbf{x}}} U_\lambda(\tilde{\mathbf{x}}_t) + \frac{\beta}{2} \nabla_{\tilde{\mathbf{x}}} \log |\mathbf{G}| + \frac{\beta}{2} \nabla_{\tilde{\mathbf{x}}} (\mathbf{p}_t^\top \mathbf{G}^{-1} \mathbf{p}_t)$ . Here, we observe that  $\mathbf{D}$  is positive semi-definite,  $\mathbf{Q}$  is anti-symmetric. Then, the desired result is a direct consequence of Theorem 1 of [38].  $\square$

## F Proof of Theorem 1

Before proving Theorem 1, we first prove the following intermediate results, whose proofs are given later in this document.

**Corollary 1.** Assume that **H1** and **H3** hold. Let  $\{\mathbf{x}_n, \mathbf{v}_n\}$  be the output our algorithm with  $\beta > 0$ . Define  $\hat{U}_N \triangleq \frac{1}{N} \sum_{n=1}^N U(\mathbf{x}_n)$ . Then the following bound holds for the bias:

$$|\mathbb{E} \hat{U}_N - \bar{U}_\beta| = \mathcal{O}\left(\frac{\beta}{Nh} + \frac{h}{\beta}\right). \quad (21)$$

**Lemma 1.** Assume that the conditions **H1** and **H2** hold. Then, the following bound holds for  $\beta \leq \frac{6}{L\pi^2} \log \frac{CL\pi^4 e}{3n}$ :

$$\bar{U}_\beta - U^* = \mathcal{O}\left(\frac{1}{\beta}\right), \quad (22)$$

where  $C$  is defined in **H2**.

### F.1 Proof of Theorem 1

*Sketch of the proof.* The proof is a direct application of Corollary 1 and Lemma 1.  $\square$

## G Proof of Corollary 1

*Sketch of the proof.* From [39][Theorem 2], the bias of a standard SG-MCMC algorithm (i.e.  $\beta = 1$ ) is bounded by

$$\mathcal{O}\left(\frac{1}{Nh'} + \frac{\sum_{n=1}^N \|\mathbb{E} \Delta V_n\|}{N} + h'\right). \quad (23)$$

where  $h'$  denotes the step-size and  $\Delta V_n$  is an operator and it is related to bias of the stochastic gradient computations if there is any. If the iterates are obtained via full gradient computations  $\nabla U$  or unbiased stochastic gradients computations (i.e. the case we consider here), then we have  $\|\mathbb{E} \Delta V_n\| = 0$ . Then by using a time-scaling argument similar to [43, 46], we define  $h = \frac{h'}{\beta}$ . This corresponds to running a standard SG-MCMC algorithm directly on the energy function  $\mathcal{E}_{\mathcal{H}}(\mathbf{x}, \mathbf{v})$ . The result is then obtained by replacing  $h'$  by  $\frac{h}{\beta}$  in (23).  $\square$

## H Proof of Lemma 1

In order to prove Lemma 1, we first need some rather elementary technical results, which we provide in Section I for clarity.

*Sketch of the proof.* We use a similar proof technique to the one given in [43][Proposition 11]. We assume that  $\pi_{\mathbf{x}}$  admits a density, denoted as  $\rho(\mathbf{x}) \triangleq \frac{1}{Z_\beta} \exp(-\beta U(\mathbf{x}))$ , where  $Z_\beta$  is the normalization constant:

$$Z_\beta \triangleq \int_{\mathcal{X}} \exp(-\beta U(\mathbf{x})) d\mathbf{x}. \quad (24)$$

We start by using the definition of  $\bar{U}_\beta$ , as follows:

$$\bar{U}_\beta = \int_{\mathcal{X}} U(\mathbf{x}) \pi_{\mathbf{x}}(d\mathbf{x}) = \frac{1}{\beta} (H(\rho) - \log Z_\beta), \quad (25)$$

where  $H(\rho)$  is the *differential entropy*, defined as follows:

$$H(\rho) \triangleq - \int_{\mathcal{X}} \rho(\mathbf{x}) \log \rho(\mathbf{x}) d\mathbf{x}. \quad (26)$$

We now aim at upper-bounding  $H(\rho)$  and lower-bounding  $\log Z_\beta$ .

By Assumption **H2**, the distribution  $\pi_{\mathbf{x}}$  has a finite second-order moment, therefore all the marginal distributions will also have bounded second order moments. By abusing the notation and denoting  $\mathbf{x} \equiv \{\mathbf{q}_1, \dots, \mathbf{q}_n, \mathbf{t}_1, \dots, \mathbf{t}_n\}$ , and by using the fact that the joint differential entropy is smaller than the sum of the differential entropies of the individual random variables, we can upper-bound  $H(\rho)$  as follows:

$$H(\rho) \leq \sum_{i=1}^n H(\rho_{\mathbf{q}_i}) + H(\rho_{\mathbf{t}_1, \dots, \mathbf{t}_n}), \quad (27)$$

where  $\rho_{\mathbf{q}_i}$  denotes the marginal density of  $\mathbf{q}_i$  and  $\rho_{\mathbf{t}_1, \dots, \mathbf{t}_n}$  denotes the joint marginal density of  $(\mathbf{t}_1, \dots, \mathbf{t}_n)$ . Since  $\rho_{\mathbf{t}_1, \dots, \mathbf{t}_n}$  is defined on  $\mathbb{R}^{3n}$ , we know that  $H(\rho_{\mathbf{t}_1, \dots, \mathbf{t}_n})$  is upper-bounded by the differential entropy of a Gaussian distribution on  $\mathbb{R}^{3n}$  that has the same second order moment. By denoting the covariance matrix of the Gaussian distribution with  $\Sigma$ , we obtain:

$$H(\rho_{\mathbf{t}_1, \dots, \mathbf{t}_n}) \leq \frac{1}{2} \log[(2\pi e)^{3n} \det(\Sigma)] \quad (28)$$

$$\leq \frac{1}{2} \log[(2\pi e)^{3n} \left(\frac{\text{tr}(\Sigma)}{3n}\right)^{3n}] \quad (29)$$

$$\leq \frac{3n}{2} \log\left(2\pi e \frac{C}{3\beta n}\right), \quad (30)$$

The equations (29) and (30) follows by the relation between the arithmetic and geometric means, and Assumption **H2**.

By using a similar argument, since  $\rho_{\mathbf{q}_i}$  lives on the unit sphere, its differential entropy is upper-bounded by the differential entropy of the uniform distribution on the unit sphere. Accordingly, we obtain:

$$H(\rho_{\mathbf{q}_i}) \leq \log(2\pi^2), \quad (31)$$

By using (30) and (31) in (27), we obtain

$$H(\rho) \leq n \log(2\pi^2) + \frac{3n}{2} \log\left(2\pi e \frac{C}{3\beta n}\right) \quad (32)$$

$$= \frac{3n}{2} \log(\sqrt{2}\pi)^{4/3} + \frac{3n}{2} \log\left(2\pi e \frac{C}{3\beta n}\right) \quad (33)$$

$$\leq \frac{3n}{2} \log\left(\frac{4\pi^3 e C}{3\beta n}\right). \quad (34)$$

We now lower-bound  $\log Z_\beta$ . By definition, we have

$$\log Z_\beta = \log \int_{\mathcal{X}} \exp(-\beta U(\mathbf{x})) d\mathbf{x} \quad (35)$$

$$= -\beta U^* + \log \int_{\mathcal{X}} \exp(\beta(U^* - U(\mathbf{x}))) d\mathbf{x} \quad (36)$$

$$\geq -\beta U^* + \log \int_{\mathcal{X}} \exp\left(-\frac{\beta L \pi^2 \|\mathbf{x} - \mathbf{x}^*\|^2}{8}\right) d\mathbf{x} \quad (37)$$

Here, in (37) we used Assumption **H1** and Corollary 2 (presented below). By using  $\mathbf{x} \equiv [\mathbf{q}_1^\top, \dots, \mathbf{q}_n^\top, \mathbf{t}^\top]^\top$  and  $\mathbf{x}^* \equiv [(\mathbf{q}_1^*)^\top, \dots, (\mathbf{q}_n^*)^\top, (\mathbf{t}^*)^\top]^\top$ , and  $\mathbf{t} \equiv [\mathbf{t}_1^\top, \dots, \mathbf{t}_n^\top]^\top$ ,  $\mathbf{t}^* \equiv [(\mathbf{t}_1^*)^\top, \dots, (\mathbf{t}_n^*)^\top]^\top$  we obtain:

$$\begin{aligned} \log Z_\beta &\geq -\beta U^* + \log \left( \prod_{i=1}^n \int_{\mathbb{S}^3} \exp\left(-\frac{\beta L \pi^2 \|\mathbf{q}_i - \mathbf{q}_i^*\|^2}{8}\right) d\mathbf{q}_i \right) \\ &\quad + \log \left( \int_{\mathbb{R}^{3n}} \exp\left(-\frac{\beta L \pi^2 \|\mathbf{t} - \mathbf{t}^*\|^2}{8}\right) d\mathbf{t} \right) \end{aligned} \quad (38)$$

$$\begin{aligned} &= -\beta U^* + \log \left( \prod_{i=1}^n \int_{\mathbb{S}^3} \exp\left(-\frac{\beta L \pi^2 \|\mathbf{q}_i - \mathbf{q}_i^*\|^2}{8}\right) d\mathbf{q}_i \right) \\ &\quad + \frac{3n}{2} \log\left(\frac{4}{\beta L \pi}\right). \end{aligned} \quad (39)$$

Let us focus on the integral with respect to  $\mathbf{q}_i$ . By definition, we have:

$$\int_{\mathbb{S}^3} \exp\left(-\frac{\beta L \pi^2 \|\mathbf{q}_i - \mathbf{q}_i^*\|^2}{8}\right) d\mathbf{q}_i = \int_{\mathbb{S}^3} \exp\left(-\frac{\beta L \pi^2}{8} (2 - 2\mathbf{q}_i^\top \mathbf{q}_i^*)\right) d\mathbf{q}_i \quad (40)$$

$$= \exp\left(-\frac{\beta L \pi^2}{4}\right) \int_{\mathbb{S}^3} \exp\left(\frac{\beta L \pi^2}{4} \mathbf{q}_i^\top \mathbf{q}_i^*\right) d\mathbf{q}_i. \quad (41)$$

By using the connection between the integral on the right hand side of the above equation and the Von Mises–Fisher distribution [69], we obtain:

$$\int_{\mathbb{S}^3} \exp\left(-\frac{\beta L \pi^2 \|\mathbf{q}_i - \mathbf{q}_i^*\|^2}{8}\right) d\mathbf{q}_i = \exp\left(-\frac{\beta L \pi^2}{4}\right) 2\pi^2 \mathcal{I}_1\left(\frac{\beta L \pi^2}{4}\right) \frac{4}{\beta L \pi^2}, \quad (42)$$

where  $\mathcal{I}_1$  denotes the modified Bessel function of the first kind. By [70] (see Equation 6.25 in the reference), we know that  $\mathcal{I}_1(x) \geq x/2$ . By using this inequality in (42), we obtain:

$$\int_{\mathbb{S}^3} \exp\left(-\frac{\beta L \pi^2 \|\mathbf{q}_i - \mathbf{q}_i^*\|^2}{8}\right) d\mathbf{q}_i \geq \exp\left(-\frac{\beta L \pi^2}{4}\right) \pi^2. \quad (43)$$

We can insert (43) in (39), as follows:

$$\log Z_\beta \geq -\beta U^* + \frac{3n}{2} \log\left(\frac{4}{\beta L \pi}\right) + \sum_{i=1}^n \log \int_{\mathbb{S}^3} \exp\left(-\frac{\beta L \pi^2 \|\mathbf{q}_i - \mathbf{q}_i^*\|^2}{8}\right) d\mathbf{q}_i \quad (44)$$

$$\geq -\beta U^* + \frac{3n}{2} \log\left(\frac{4}{\beta L \pi}\right) - n \frac{\beta L \pi^2}{4} + 2n \log \pi \quad (45)$$

$$\geq -\beta U^* + \frac{3n}{2} \log\left(\frac{4}{\beta L \pi}\right) - n \frac{\beta L \pi^2}{4} \quad (46)$$

Finally, by combining (25), (34), and (46), we obtain:

$$\bar{U}_\beta - U^* = \frac{1}{\beta} (H(\rho) - \log Z_\beta) - U^* \quad (47)$$

$$\leq \frac{3n}{2\beta} \log\left(\frac{4\pi^3 e C}{3\beta n}\right) - \frac{3n}{2\beta} \log\left(\frac{4}{\beta L \pi}\right) + n \frac{L \pi^2}{4} \quad (48)$$

$$= \frac{3n}{2\beta} \log\left(\frac{C L \pi^4 e}{3n}\right) + n \frac{L \pi^2}{4} \quad (49)$$

$$\leq \frac{3n}{\beta} \log\left(\frac{C L \pi^4 e}{3n}\right). \quad (50)$$

The last line follows from the hypothesis. This finalizes the proof.  $\square$

## I Technical Results

In the following lemma, we generalize [71][Lemma 1.2.3] to manifolds. Similar arguments can be found in [54, 55].

**Lemma 2.** *Let  $\mathcal{X} \subset \mathbb{R}^n$  be a Riemannian manifold with metric  $d_{\mathcal{X}}$ , and let  $\gamma : [0, 1] \mapsto \mathcal{X}$  be a constant-speed geodesic curve between two points  $\mathbf{x}, \mathbf{y} \in \mathcal{X}$ , such that  $\gamma(0) = \mathbf{x}$  and  $\gamma(1) = \mathbf{y}$ . Let  $f : \mathcal{X} \mapsto \mathbb{R}$  be a continuously differentiable function with Lipschitz continuous gradients. Then the following bound holds for every  $\mathbf{x}, \mathbf{y} \in \mathcal{X}$ :*

$$\left| f(\mathbf{y}) - f(\mathbf{x}) - \int_0^1 \langle \nabla f(\mathbf{x}), \gamma'(t) \rangle dt \right| \leq \frac{L}{2} d_{\mathcal{X}}(\mathbf{x}, \mathbf{y})^2, \quad (51)$$

where  $\langle \mathbf{x}, \mathbf{y} \rangle \triangleq \mathbf{x}^\top \mathbf{y}$  and  $L$  denotes the Lipschitz constant.

*Sketch of the proof.* Let us define a function  $\varphi : [0, 1] \mapsto \mathbb{R}$ , such that  $\varphi(t) \triangleq f(\gamma(t))$ . By definition, we have  $\varphi(0) = f(\mathbf{x})$  and  $\varphi(1) = f(\mathbf{y})$ . By using the second fundamental theorem of calculus, we can write:

$$\varphi(1) - \varphi(0) = \int_0^1 \varphi'(t) dt, \quad (52)$$

where  $\varphi'(t)$  denotes the derivative of  $\varphi(t)$  with respect to  $t$ . By the theorem of derivation of composite functions, we have

$$\varphi'(t) = \langle \nabla f(\gamma(t)), \gamma'(t) \rangle. \quad (53)$$

By combining (52) and (53), we obtain the following identity for all  $\mathbf{x}, \mathbf{y} \in \mathcal{X}$ :

$$f(\mathbf{y}) = f(\mathbf{x}) + \int_0^1 \langle \nabla f(\gamma(t)), \gamma'(t) \rangle dt \quad (54)$$

$$= f(\mathbf{x}) + \int_0^1 \langle \nabla f(\mathbf{x}), \gamma'(t) \rangle dt + \int_0^1 \langle \nabla f(\gamma(t)) - \nabla f(\mathbf{x}), \gamma'(t) \rangle dt. \quad (55)$$

Therefore, we obtain

$$\left| f(\mathbf{y}) - f(\mathbf{x}) - \int_0^1 \langle \nabla f(\mathbf{x}), \gamma'(t) \rangle dt \right| = \left| \int_0^1 \langle \nabla f(\gamma(t)) - \nabla f(\mathbf{x}), \gamma'(t) \rangle dt \right| \quad (56)$$

$$\leq \int_0^1 \left| \langle \nabla f(\gamma(t)) - \nabla f(\mathbf{x}), \gamma'(t) \rangle \right| dt \quad (57)$$

$$\leq \int_0^1 \|\nabla f(\gamma(t)) - \nabla f(\mathbf{x})\| \|\gamma'(t)\| dt \quad (58)$$

$$\leq L \int_0^1 d_{\mathcal{X}}(\gamma(t), \mathbf{x}) \|\gamma'(t)\| dt. \quad (59)$$

We can now use the fact that the geodesic curve has a constant velocity, such that  $\|\gamma'(t)\| = d_{\mathcal{X}}(\mathbf{x}, \mathbf{y})$  for all  $t \in [0, 1]$ , which also implies  $d_{\mathcal{X}}(\gamma(t_1), \gamma(t_2)) = |t_1 - t_2| d_{\mathcal{X}}(\gamma(1), \gamma(0))$ . Then, using  $\mathbf{x} = \gamma(0)$ ,  $\mathbf{y} = \gamma(1)$ , we obtain:

$$\left| f(\mathbf{y}) - f(\mathbf{x}) - \int_0^1 \langle \nabla f(\mathbf{x}), \gamma'(t) \rangle dt \right| \leq L \int_0^1 t d_{\mathcal{X}}(\mathbf{x}, \mathbf{y})^2 dt \quad (60)$$

$$= \frac{L}{2} d_{\mathcal{X}}(\mathbf{x}, \mathbf{y})^2. \quad (61)$$

This concludes the proof.  $\square$

**Corollary 2.** *Under the assumptions of Lemma 2, the following bound holds for all  $\mathbf{x} \in \mathcal{X}$*

$$f(\mathbf{x}) - f^* \leq \frac{L\pi^2}{8} \|\mathbf{x} - \mathbf{x}^*\|^2, \quad (62)$$

where  $\mathcal{X} \triangleq (\mathbb{S}^3)^n \times \mathbb{R}^{3n}$ ,  $f^* = \min_{\mathbf{x}' \in \mathcal{X}} f(\mathbf{x}')$  and  $\mathbf{x}^* = \arg \min_{\mathbf{x}' \in \mathcal{X}} f(\mathbf{x}')$ .

*Sketch of the proof.* By using Lemma 2 and the obvious facts that  $\nabla f(\mathbf{x}^*) = 0$  and  $f(\mathbf{x}) > f^*$  for all  $\mathbf{x} \in \mathcal{X}$ , we have:

$$f(\mathbf{x}) - f^* \leq \frac{L}{2} d_{\mathcal{X}}(\mathbf{x}, \mathbf{x}^*)^2. \quad (63)$$

The inequality given in Equation A.1.1 in [72] states that the geodesic distance on the sphere is bounded by the 2-norm, more precisely, for all  $\mathbf{q}, \mathbf{q}' \in \mathbb{S}^{d-1}$  we have:

$$d_{\mathbb{S}^{d-1}}(\mathbf{q}, \mathbf{q}') \leq \frac{\pi}{2} \|\mathbf{q} - \mathbf{q}'\|. \quad (64)$$

Using  $\mathbf{x} \equiv [\mathbf{q}_1^\top, \dots, \mathbf{q}_n^\top, \mathbf{t}_1^\top, \dots, \mathbf{t}_n^\top]^\top$  and  $\mathbf{x}^* \equiv [(\mathbf{q}_1^*)^\top, \dots, (\mathbf{q}_n^*)^\top, (\mathbf{t}_1^*)^\top, \dots, (\mathbf{t}_n^*)^\top]^\top$  yields:

$$f(\mathbf{x}) - f^* \leq \frac{L}{2} \left( \sum_{i=1}^n d_{\mathbb{S}^3}(\mathbf{q}_i, \mathbf{q}_i^*)^2 + \sum_{i=1}^n \|\mathbf{t}_i - \mathbf{t}_i^*\|^2 \right) \quad (65)$$

$$\leq \frac{L}{2} \left( \frac{\pi^2}{4} \sum_{i=1}^n \|\mathbf{q}_i - \mathbf{q}_i^*\|^2 + \sum_{i=1}^n \|\mathbf{t}_i - \mathbf{t}_i^*\|^2 \right) \quad (66)$$

$$\leq \frac{L\pi^2}{8} \left( \sum_{i=1}^n \|\mathbf{q}_i - \mathbf{q}_i^*\|^2 + \sum_{i=1}^n \|\mathbf{t}_i - \mathbf{t}_i^*\|^2 \right) \quad (67)$$

$$= \frac{L\pi^2}{8} \|\mathbf{x} - \mathbf{x}^*\|^2. \quad (68)$$

This concludes the proof.  $\square$

## J Gradients of Likelihood and Prior Terms

In this section we provide derivations of the gradients for data and prior terms. For completeness, we find it worthy to once again repeat our MLE formulation:

$$\arg \max_{\mathbf{Q}, \mathbf{T}} \left( \sum_{(i,j) \in E} \{ \log p(\mathbf{q}_{ij} | \mathbf{Q}, \mathbf{T}) + \log p(\mathbf{t}_{ij} | \mathbf{Q}, \mathbf{T}) \} + \sum_i \log p(\mathbf{q}_i) + \sum_i \log p(\mathbf{t}_i) \right). \quad (69)$$

We begin by deriving the gradients of the **rotational components** first, and translations second. In the setting where  $\mathbf{V}$  is constant w.r.t.  $\mathbf{q}$  the gradient of log Bingham distribution w.r.t. the random variable  $\mathbf{q}$  reads:

$$\nabla_{\mathbf{x}} \log \mathcal{B}(\mathbf{x}; \mathbf{\Lambda}, \mathbf{V}) = \nabla_{\mathbf{x}} \log \frac{1}{F} + \nabla_{\mathbf{x}} (\mathbf{x}^T \mathbf{V} \mathbf{\Lambda} \mathbf{V}^T \mathbf{x}) = (\mathbf{V} \mathbf{\Lambda} \mathbf{V}^T + \mathbf{V} \mathbf{\Lambda}^T \mathbf{V}^T) \mathbf{x} = 2\mathbf{V} \mathbf{\Lambda} \mathbf{V}^T \mathbf{x}. \quad (70)$$

As the first column of  $\mathbf{V}$  is the mode, we avoid storing it. Thus, for the implementation purposes, we abuse the notation and use  $\mathbf{V} \in \mathbb{R}^{4 \times 3}$  and  $\mathbf{\Lambda} \in \mathbb{R}^{3 \times 3}$ . Normalizing constant  $F$  drops as it depends on  $\mathbf{\Lambda}$  only [73]. We also have cases where  $\mathbf{V}$  is a function of the mode  $\mathbf{q}$ ,  $\mathbf{V} \rightarrow \mathbf{V}(\mathbf{q})$ . Then:

$$\nabla_{\mathbf{q}} \log \mathcal{B}(\mathbf{x}; \mathbf{\Lambda}, \mathbf{V}(\mathbf{q})) = \nabla_{\mathbf{q}} (\mathbf{x}^T \mathbf{V}(\mathbf{q}) \mathbf{\Lambda} \mathbf{V}^T(\mathbf{q}) \mathbf{x}) = \nabla_{\mathbf{k}} (\mathbf{k}^T \mathbf{\Lambda} \mathbf{k}) \nabla_{\mathbf{q}}(\mathbf{k}) = 2\mathbf{k}^T \mathbf{\Lambda} \nabla_{\mathbf{q}}(\mathbf{k}), \quad (71)$$

where  $\mathbf{k} = \mathbf{V}^T(\mathbf{q}) \mathbf{x} \in \mathbb{R}^3$  is used to ease the computations. Note that in our particular application it is the case that  $\mathbf{x} \leftarrow \mathbf{q}_{ij}$ , i.e. the data is specified by the relative poses attached to the edges of the graph. We then speak of the gradient of  $\log(p(\mathbf{q}_{ij} | \mathbf{q}_i, \mathbf{q}_j))$  with  $\mathbf{V} \rightarrow \mathbf{V}(\mathbf{q}_j \bar{\mathbf{q}}_i)$  w.r.t.  $\mathbf{q}_i$ . We shorten  $\mathbf{r} \leftarrow \mathbf{q}_j \bar{\mathbf{q}}_i$  and write  $\mathbf{V}$  as a function of  $\mathbf{r}$ ,  $\mathbf{V}(\mathbf{r}) \triangleq \mathbf{V}(\mathbf{q}_j \bar{\mathbf{q}}_i)$ . Then:

$$\nabla_{\mathbf{q}_i} \log \mathcal{B}(\mathbf{x}; \mathbf{\Lambda}, \mathbf{V}(\mathbf{r})) = \nabla_{\mathbf{r}} \log \mathcal{B}(\mathbf{x}; \mathbf{\Lambda}, \mathbf{V}(\mathbf{r})) \nabla_{\mathbf{q}_i}(\mathbf{r}) = 2\mathbf{k}^T \mathbf{\Lambda} \nabla_{\mathbf{r}}(\mathbf{k}) \nabla_{\mathbf{q}_i}(\mathbf{r}), \quad (72)$$

this time with  $\mathbf{k} = \mathbf{V}^T(\mathbf{r}) \mathbf{x} \in \mathbb{R}^3$ . Note that  $\nabla_{\mathbf{r}} \log \mathcal{B}(\mathbf{x}; \mathbf{\Lambda}, \mathbf{V}(\mathbf{r}))$  is expanded as in Eq. 71. Using the definition of  $\mathbf{V}$  in Eq. 3, the terms simplify to:

$$\mathbf{k} = \begin{bmatrix} q_1 x_2 - q_2 x_1 + q_3 x_4 - q_4 x_3 \\ q_1 x_3 - q_3 x_1 - q_2 x_4 + q_4 x_2 \\ -q_1 x_4 - q_2 x_3 + q_3 x_2 + q_4 x_1 \end{bmatrix} \quad \nabla_{\mathbf{q}}(\mathbf{k}) = \begin{bmatrix} x_2 & -x_1 & x_4 & -x_3 \\ x_3 & -x_4 & -x_1 & x_2 \\ x_4 & x_3 & -x_2 & -x_1 \end{bmatrix}. \quad (73)$$

The last term in eq. 72 expands as:

$$\nabla_{\mathbf{q}_i}(\mathbf{q}_j \bar{\mathbf{q}}_i) = \begin{bmatrix} q_{j,1} & q_{j,2} & q_{j,3} & q_{j,4} \\ q_{j,2} & -q_{j,1} & q_{j,4} & -q_{j,3} \\ q_{j,3} & -q_{j,4} & -q_{j,1} & q_{j,2} \\ q_{j,4} & q_{j,3} & -q_{j,2} & -q_{j,1} \end{bmatrix}. \quad (74)$$

Due to the symmetry of the relative poses in the graph, we do not need to compute the gradients w.r.t.  $\mathbf{q}_j$ . We will now derive the gradients for **translational components**. Similarly, we start by the gradient of the log likelihood w.r.t. the data. While a shorter derivation through matrix calculus is also possible, we deliberately provide a longer version, as it might be more intuitive:

$$\begin{aligned} \nabla_{\mathbf{t}} \log \mathcal{N}(\mathbf{t}; \boldsymbol{\mu}, \sigma^2 \mathbf{I}) &= \nabla_{\mathbf{t}} \log \frac{1}{G} + \nabla_{\mathbf{t}} \left( -\frac{1}{2} (\mathbf{t} - \boldsymbol{\mu})^T \boldsymbol{\Sigma}^{-1} (\mathbf{t} - \boldsymbol{\mu}) \right) \\ &= \nabla_{\mathbf{t}} \left( -\frac{1}{2} (\mathbf{t}^T \boldsymbol{\Sigma}^{-1} \mathbf{t} - \mathbf{t}^T \boldsymbol{\Sigma}^{-1} \boldsymbol{\mu} - \boldsymbol{\mu}^T \boldsymbol{\Sigma}^{-1} \mathbf{t} + \boldsymbol{\mu}^T \boldsymbol{\Sigma}^{-1} \boldsymbol{\mu}) \right) \\ &= -\frac{1}{2} (\mathbf{t}^T (\boldsymbol{\Sigma}^{-1} + \boldsymbol{\Sigma}^{-T}) - (\boldsymbol{\Sigma}^{-1} \boldsymbol{\mu})^T - (\boldsymbol{\mu}^T \boldsymbol{\Sigma}^{-1}) + 0) \\ &= -\frac{1}{2} (2\mathbf{t}^T \boldsymbol{\Sigma}^{-1} - 2\boldsymbol{\mu}^T \boldsymbol{\Sigma}^{-1}) = (\boldsymbol{\mu}^T - \mathbf{t}^T) \boldsymbol{\Sigma}^{-1} \end{aligned} \quad (75)$$

The normalizing constant drops similarly as it does not depend on  $\mathbf{t}$ .

Similar to rotational counterpart, our algorithm centers the data on the mean of the distribution, also requiring to compute the gradients w.r.t. the mean of the distribution. With a derivation similar to but simpler from Eq. 75, it follows:

$$\nabla_{\boldsymbol{\mu}} \log \mathcal{N}(\mathbf{x}; \boldsymbol{\mu}, \sigma^2 \mathbf{I}) = -\frac{1}{2} (2\boldsymbol{\mu}^T \boldsymbol{\Sigma}^{-1} - 2\mathbf{x}^T \boldsymbol{\Sigma}^{-1}) = (\mathbf{x}^T - \boldsymbol{\mu}^T) \boldsymbol{\Sigma}^{-1} \quad (76)$$

When we center the distribution on the data, substituting  $\boldsymbol{\mu} \leftarrow \mathbf{t}_j - \mathbf{r} \mathbf{t}_i \bar{\mathbf{r}}$ , where  $\mathbf{r} \leftarrow \mathbf{q}_j \bar{\mathbf{q}}_i$ ,  $\mathbf{x} \leftarrow \mathbf{t}_{ij}$ , we arrive at:

$$\nabla_{\mathbf{t}_i} \log \mathcal{N}(\mathbf{x}; \boldsymbol{\mu}, \sigma^2 \mathbf{I}) = \nabla_{\boldsymbol{\mu}} \log \mathcal{N}(\mathbf{x}; \boldsymbol{\mu}, \sigma^2 \mathbf{I}) \mathbf{J}_{\mathbf{t}_i}(\boldsymbol{\mu}) \quad (77)$$

Note that the first term of the right hand side is given in Eq. 76. The second one can be computed from the derivative of the sandwich action on the 1-blade  $\mathbf{t}_i$ . With slight abuse of notation, in the following we assume that translation-quaternion is purified:  $\mathbf{t}_i \leftarrow [0; \mathbf{t}_i]$ .

$$\mathbf{J}_{\mathbf{t}_i}(\boldsymbol{\mu}) = \mathbf{J}_{\mathbf{t}_i}(\mathbf{t}_j - \mathbf{r} \mathbf{t}_i \bar{\mathbf{r}}) \quad (78)$$

$$= -\mathbf{J}_{\mathbf{t}_i} \left( Q(\bar{\mathbf{r}}) Q(\mathbf{t}_i) \mathbf{r}^T \right) \quad (79)$$

$$= -\mathbf{J}_{\mathbf{t}_i} \left( (\mathbf{q}_{ij} \otimes Q(\bar{\mathbf{r}})) \text{vec}(Q(\mathbf{t}_i)) \right) \quad (80)$$

$$= -\mathbf{J}_{\mathbf{t}_i} \left( \mathbf{K} \text{vec}(Q(\mathbf{t}_i)) \right) \quad (81)$$

$$= -\mathbf{K} \nabla_{\mathbf{t}_i} \text{vec}(Q(\mathbf{t}_i)) \quad (82)$$

$$= -\mathbf{K} \mathbf{J}_{\mathbf{t}_i} \quad (83)$$

$$= \begin{bmatrix} 0 & 0 & 0 \\ -q_1^2 - q_2^2 + q_3^2 + q_4^2 & 2q_1 q_4 - 2q_2 q_3 & -2q_1 q_3 - 2q_2 q_4 \\ -2q_1 q_4 - 2q_2 q_3 & -q_1^2 + q_2^2 - q_3^2 + q_4^2 & 2q_1 q_2 - 2q_3 q_4 \\ 2q_1 q_3 - 2q_2 q_4 & -2q_1 q_2 - 2q_3 q_4 & -q_1^2 + q_2^2 + q_3^2 - q_4^2 \end{bmatrix} \quad (84)$$

where  $\mathbf{K} \in R^{4 \times 16}$  refers to the Kronecker product matrix  $\mathbf{K} = \mathbf{r} \otimes Q(\bar{\mathbf{q}}_{ij})$ ,  $\mathbf{J}_{\mathbf{t}_i} = \nabla_{\mathbf{t}_i} \text{vec}(Q(\mathbf{t}_i))$  is the  $16 \times 3$  Jacobian matrix and  $\text{vec}(\cdot)$  denotes the linearization operator. Individual components  $q_i$  belong to  $\mathbf{r} = [q_1, q_2, q_3, q_4]$ . The map  $Q(\cdot) : \mathbb{H}_1 \rightarrow R^{4 \times 4}$  constructs a Quaternion matrix form:

$$Q(\mathbf{q}) = \begin{bmatrix} q_1 & -q_2 & -q_3 & -q_4 \\ q_2 & q_1 & q_4 & -q_3 \\ q_3 & -q_4 & q_1 & q_2 \\ q_4 & q_3 & -q_2 & q_1 \end{bmatrix} \quad (85)$$

leading to a more compact notation of the quaternion product. In fact this is not very different from the definition of  $\mathbf{V}(\mathbf{q})$ , as one is free to pick any of the 48 distinct representations out of the matrix ring  $\mathbb{M}(4, \mathbb{R})$ . For a more thorough reading on differentiating the quaternions, we refer the reader to [74]. Note that Eq. 84 has zeros in the initial row. This is due to the property that all the operations respect the purity of the blade. The final Jacobian matrix can be extracted from the remaining three rows corresponding to the vector part.

Last but not least, we require the gradients of the translational part w.r.t. the quaternions due to the coupling:

$$\nabla_{\mathbf{q}_i} \log \mathcal{N}(\mathbf{x}; \boldsymbol{\mu}, \sigma^2 \mathbf{I}) = \nabla_{\boldsymbol{\mu}} \log \mathcal{N}(\mathbf{x}; \boldsymbol{\mu}, \sigma^2 \mathbf{I}) J_{\mathbf{q}_i}(\boldsymbol{\mu}) \quad (86)$$

The first term in Eq. 86 is given above and the derivation of the rightmost Jacobian is subject to an operation similar to the ones given in 78.

## K Additional Experiments and Details

**Hyper-parameter Selection** Throughout all the experiments we set  $c \leftarrow 1000$  and during optimization  $\beta \leftarrow \infty$ . In practice, we only set  $\beta$  to a very large finite value.  $h$  varies between  $0.001 - 0.008$  depending on the dataset  $((\lambda, \sigma^2))$ . We typically set Bingham and Gaussian variances to be at the noise level of the dataset, evaluated empirically. The variance of the Bingham distribution is  $\lambda \in [350, 900]$ . Likewise, variance of the Gaussian lies in  $\sigma^2 \in [0.01, 0.1]$ . To show that the choice is not critical, in Fig. 6, we plot  $\lambda$ , our most sensitive parameter, against the error attained at convergence for different datasets, including synthetic and real. The figure indicates that for a variety of choices,  $\lambda > 100$ , the solution can safely be found. Note that certain level of noise can also be compensated by the step size, as variance and step size are multiplicative factors. Moreover, the step size can be adjusted dynamically proportional to the dataset size. The number of integration steps varies, typically in range  $[350, 800]$  and TG-MCMC runs until convergence.

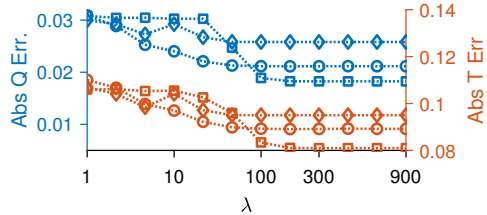


Figure 6: Effect of  $\lambda$  on rotational (**Q**) and translational (**T**) errors.

**Graph Consistency** In the paper, as well as in this supplementary material, we speak of *graph consistency*, an intuitive measure of quantifying how well the estimated parameters agree to the input data. This measure is easier to interpret than, say, average rotational distance, that is always unit bound. We define the graph consistency as follows:

$$g_c = 1 - \frac{1}{\pi|E|} \sum_{(i,j) \in E} 2 \arccos(\mathbf{q}_{ij}(\mathbf{q}_i \bar{\mathbf{q}}_j)) \quad (87)$$

In other words,  $g_c$  measures how well the relative poses computed from absolute estimates align with the ones given in the data.  $g_c = 1$  for the perfect ground truth and  $g_c \rightarrow 0$  when all estimates are off by  $\pi$ .

### K.1 Quantitative Evaluations

**Outliers** Even though TG-MCMC has no explicit treatment of outliers, it is still of interest to observe the robustness to outliers. We do that synthetically, by following a similar experimentation setup to the main paper. This time, we increase the outlier ratio in the pose graph by excessively corrupting some of the relative transformation matrices by composing it with random rotations in the range  $[60^\circ 80^\circ]$  around random axes, and random translations between  $[0, 1]$ . We then run TG-MCMC, as well as the other algorithms under consideration. Our results are depicted in Fig. 7. Many state-of-the-art methods that lack outlier handling are similar in performance. However, advantage of TG-MCMC is more apparent as the outlier percentage increases.

**Projected Gradient Descent** Next, we compare our method against projected gradient descent (PGD) algorithm, that is heavily used when one avoids the manifold operations of quaternions. This



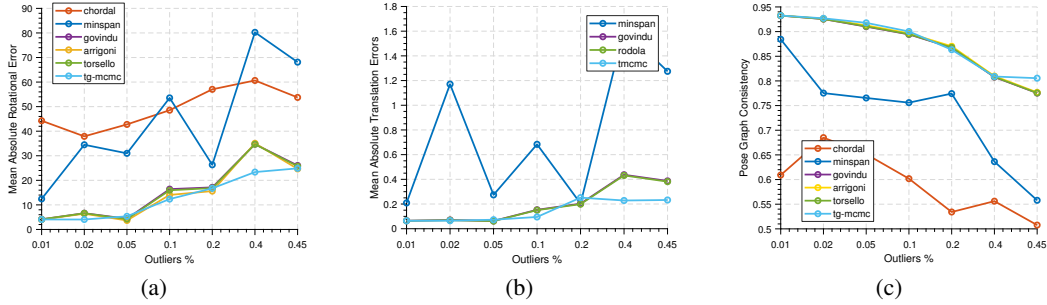


Figure 7: Robustness to outliers. With respect to the outlier percentage, we plot: **(a)** deviations of rotations from ground truth (mean error) **(b)** deviations of translation from ground truth (mean error) **(c)** graph consistency (for definition, see paper).

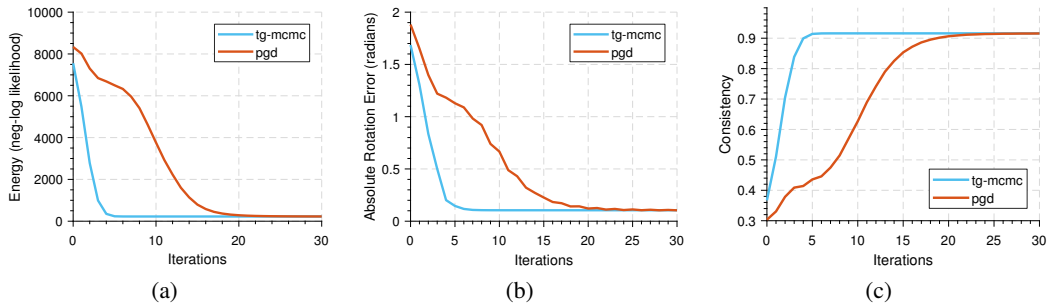


Figure 8: Synthetic evaluations against projected gradient descent (PGD). **(a)** Iterations vs negative log likelihood **(b)** Iterations vs absolute rotation error of the estimates w.r.t. ground truth. **(c)** Iterations vs consistency (for definition, see paper).

amounts to solving our MAP estimation using a standard first order method and projecting the intermediary solutions back onto the manifold. Using compatible step sizes, Fig. 8 plots multiple quantities as iterates progress. It is clearly visible that walking on the manifold is advantageous both in finding quicker solutions (a,b) and reducing the energy of the cost (c).

**Runtime Performance** We now provide, in Tab. 2a runtime analysis. It is common to all PGO initialization algorithms to outperform BA in terms of speed, which justifies the attempt to initialize PGO. Among the compared methods, we are not the fastest. Our runtimes are just comparable to those of the state of the art. However, we have, in addition, the component of uncertainty estimates, which cannot be provided by the competing algorithms. It is also clearly visible that BA benefits from the TG-MCMC initialization by an order of magnitude (shown in Gains column).

Table 2: Runtimes (seconds) of different algorithms. BA-X refers to BA with initialization X. *Points*, *Poses* refer to optimizing only points or only poses, respectively.

| Dataset        | PGO      |          |         |       | BA-MinSpan |       | BA-Ours |       | Gains         |
|----------------|----------|----------|---------|-------|------------|-------|---------|-------|---------------|
|                | Arrigoni | Torsello | Govindu | Ours  | Points     | Poses | Points  | Poses |               |
| Madrid         | 0.137    | 2.255    | 3.033   | 5.794 | 53.82      | 139.6 | 33.30   | 14.54 | <b>9.60x</b>  |
| South Building | 0.060    | 0.784    | 1.213   | 1.986 | 46.18      | 108.0 | 6.087   | 4.969 | <b>21.74x</b> |

## K.2 Qualitative Evaluations

**Uncertainty Estimation** We now give further visualizations showing the behavior of uncertainty estimation. Let us first supplement the main paper, by providing close up and easier to view shots of some of the scenes. Due to space limitations, we had to omit some of the larger drawings from the main paper. Fig. 9 illustrates the uncertainty mapping on the Madrid Metropolis reconstruction and Fig. 10 on the South Building dataset [75, 76]. In the former, distant content, which is intrinsically

less accurate to triangulate, appears less certain than the structure nearby. This overlaps well with the findings of stereo vision where baseline-to-distance ratio determines the triangulation accuracy. In the latter, though, we see that hard to match content such as vegetation has more uncertainty. This is also natural, because such image regions render the feature matching difficult. Finally, we provide uncertainty maps for two more objects Angel and Fountain. In these objects, due to the small size and noise, uncertainty variation is less apparent and hard to observe. However, on Angel, our algorithm overall manages to spot the noisy points and mark them with higher uncertainty. On the Fountain, the structure close to the borders of the image are shot from a fewer number of cameras, which is what TG-MCMC has discovered.

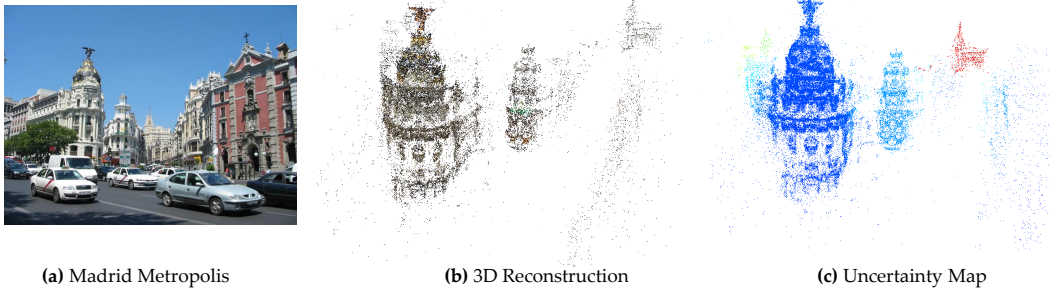


Figure 9: Reconstruction of Madrid Metropolis. Our uncertainty map can reveal the distant structure such as buildings because the 3D triangulation quality decreases with the distance. Samples produced by TG-MCMC can successfully explain these variations.

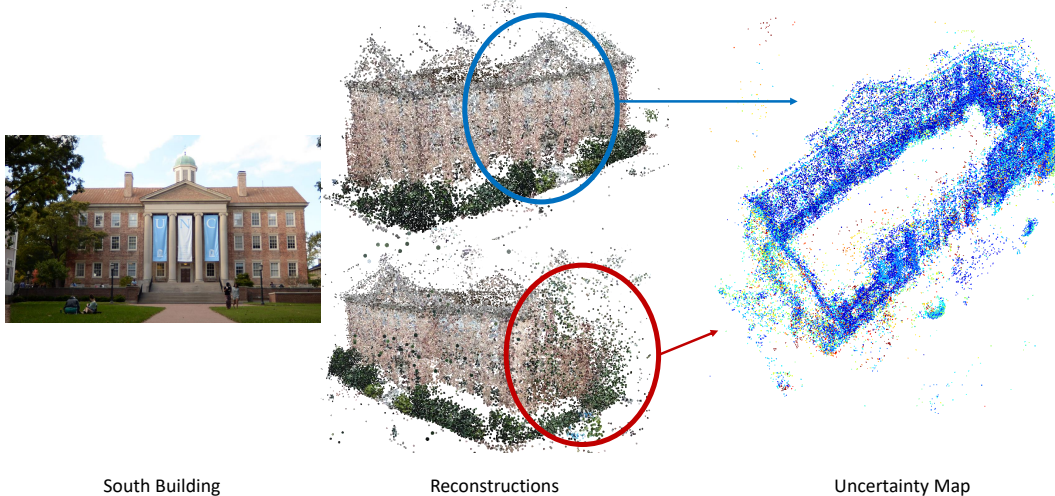


Figure 10: Reconstruction of South Building of UNC. Notice that hard-to-reconstruct structure such as vegetation is also marked to be uncertain by our algorithm, whereas rigid structures such as building façades enjoy high certainty.



Figure 11: Uncertainty visualizations on Angel and Fountain objects.

**Graph Evolution** To shed light upon the inner workings of TG-MCMC, we now visualize the evolution of the pose graph as iterations/time proceed(s). Fig. 12 presents snapshots of the pose graph of Angel dataset, evolving towards the solution. Notice, our algorithm can start from a random initialization and achieve results that are very close to the ground truth. In fact, we also show

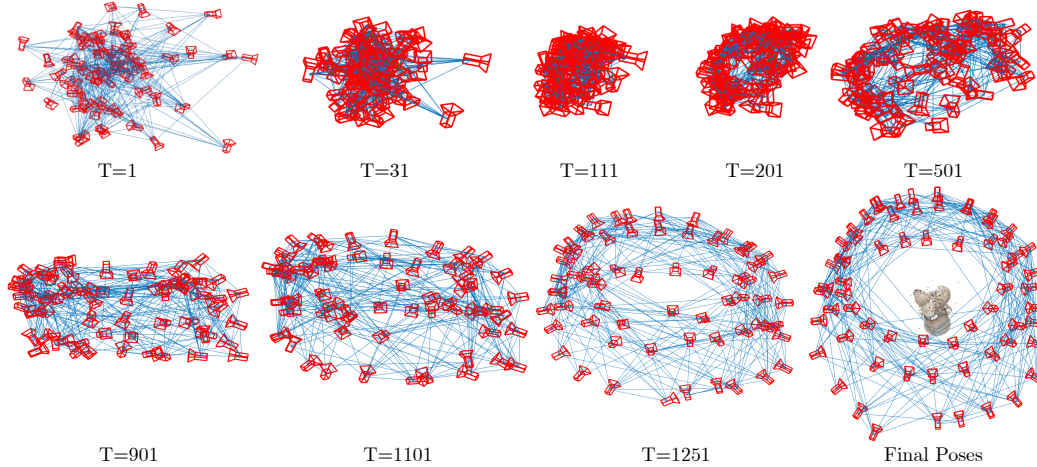


Figure 12: Evolution of the graph structure on the Angel object.

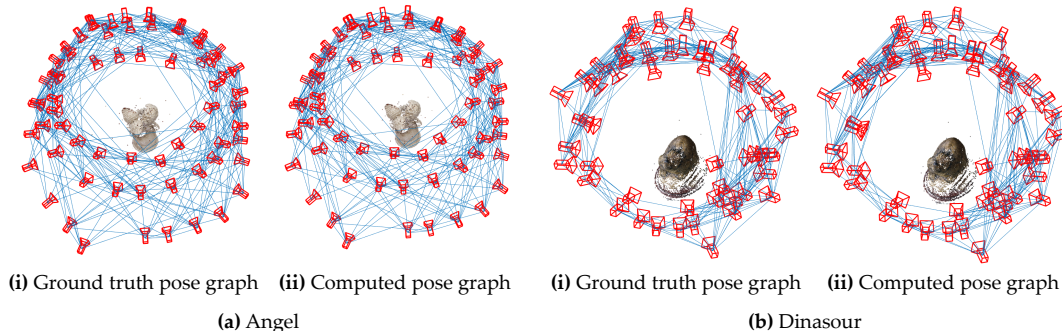


Figure 13: Comparing the resulting pose graph with the ground truth for Angel and Dino objects.

comparisons of the obtained pose graph against the ground truth poses in Fig. 13. Our low numbers in quantitative error well transfers to qualitative evaluations.

**Further Visual Results from the Used Datasets** In order to have a better idea of the nature of the datasets we utilized, it is worthwhile to visualize the camera locations as well as the 3D reconstruction following a full bundle adjustment, that optimizes both 3D points (structure) and 3D poses (motion). In Fig. 14, we report 6 such visualizations on 3 outdoor, large scenes, as well as 3 object-scanning scenarios. These plots are not the outcome of our approach, but meant as a reference for the datasets we deal with.

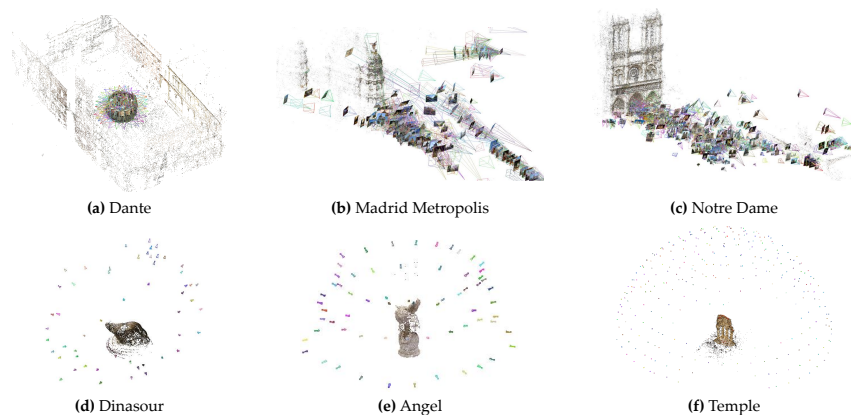


Figure 14: Results of the full bundle adjustment (structure + camera poses) on several datasets.